

Recent progress and strategies on mixed-dimensional heterostructures for potassium-ion storages

Yi-Yen Hsieh ¹, Hsing-Yu Tuan ^{1,*}

Department of Chemical Engineering, National Tsing Hua University, Hsinchu, 30013, Taiwan



ARTICLE INFO

Article history:

Received 9 February 2022

Received in revised form

23 March 2022

Accepted 3 April 2022

Available online 25 April 2022

Keywords:

Mixed-dimensional

Heterostructure

Heterointerface engineering

Multidimension

Potassium-ion storage

ABSTRACT

Renewable potassium-ion energy storage shows attractive potential due to high-discharge platform and sufficient energy density, with outstanding advantages of abundant reserves and cost-effectiveness. However, key anode materials face various bottlenecks and formidable challenges, such as poor electrical conductivity, low ionic diffusivity, sluggish interfacial/surface reaction, and severe volume expansion, which distinctly inhibit the electrochemical performance of potassium-ion system. The construction of heterostructures can synergistically improve the deficiencies and combine the unique functionalities of different materials to enhance the potassium-ion storage capacity of metal chalcogenides or oxides. In this review, understandings and insights into the diffusion and kinetic behavior of mixed-dimensional heterostructures (MDHs) will be systematically discussed and revealed. Furthermore, these benefits and merits will be maximized and optimized, accompanied by recent state-of-the-art synthetic strategies and characterization techniques. Finally, we propose improvements and perspectives for the feasible development of heterostructures in next-generation energy storage systems.

© 2022 Elsevier Ltd. All rights reserved.

1. Introduction

Nowadays, a lot of attention has been shed on the prevention of environmental pollution and exploiting renewable resources to diminish the continuous consumption of limited supply of fossil fuels. Exploring the sustainable and reliable energy storages is the key to effectively reserving the renewable energy sources, including wind, geothermal, solar, and other renewable energy sources. Therefore, there is an urgent need to develop low-cost, high-energy-density, and high-performance rechargeable storage systems to meet the growing demand for electrochemical energy storage in large-scale power grids [1,2]. Due to the limited availability of lithium resources, potassium-ion batteries (PIBs) have gained considerable attention, which are similar in principle and technique to the well-established lithium-ion batteries (LIBs) [3]. Metals with high theoretical capacity (e.g. antimony, bismuth, and its alloy [4]), metal chalcogenides (e.g. sulfides, selenides), and metal oxides are often selected as anode materials for PIBs. However, the single-phase materials suffer from poor ion diffusivity,

wide bandgap, poor electrical conductivity, severe volume variation, and sluggish interfacial/surface reaction (Fig. 1a), which significantly limit the electrochemical performances [5].

In recent years, most of the reported literature have adopted three common concepts, synergistic effects, nano-crystallization effects, and morphology modification (Fig. 2). Compared with single-component active materials, the synergistic effect resulted from the multi-constituents and their different redox voltage of conversion-type, alloy-type, and even the composite materials (e.g. BiSb@P [6], SnSb@C [7]), which can alleviate the drastic phase transition and decrease the possibility of materials fragmentation during cyclic testing. Furthermore, the introduction of conversion-alloying dual mechanism materials in carbon scaffolds can form a stable solid electrolyte interphase (SEI), which prevents the continuous fracture and reformation of the SEI layer and guarantees the eminent structural stability and cycling performances in PIBs [8]. As the size of active materials is reduced to nanoscale, the diffusion paths and ion/electron transport are reduced and facilitated, respectively, due to nano-crystallization effect. In addition to decreasing the size of bulks and micromaterials to nanosized structures, the intrinsic properties and rate capability of electrodes can also be enhanced via morphology modification with different dimensionality, including nanosheet [9], nanoteardrop [10], nanowire [11], and nanonetwork [12].

* Corresponding author.

E-mail address: hytuan@che.nthu.edu.tw (H.-Y. Tuan).

¹ This minireview is written by Yi-Yen Hsieh and Hsing-Yu Tuan with data cited from the literature.

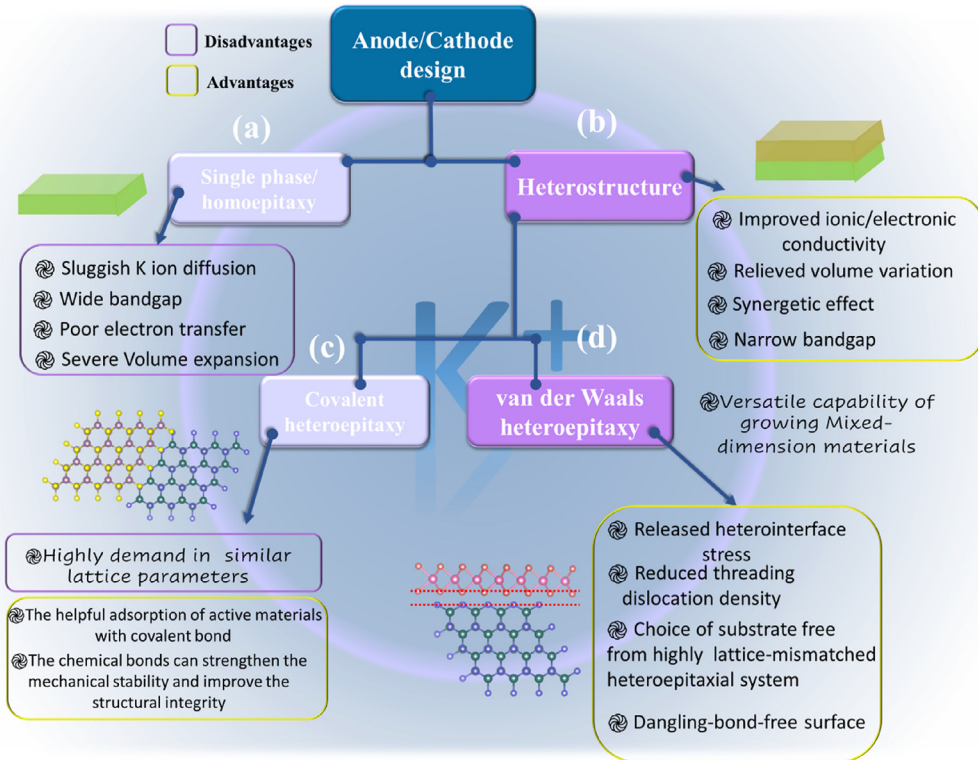


Fig. 1. Schematic illustration of the heterostructure and its advantages and disadvantages.

Although the above strategies enhance the electrochemical storage capacity, the interfacial properties of the materials still cannot meet the requirements of PIBs. Therefore, the construction and modification of heterojunctions have a crucial impact on improving the storage capability and enhancing the structural stability. Based on synergistic effects, nanocrystalline effects, and morphology modification, the use of nanomaterials to design and engineer heterostructures of different sizes can improve interfacial diffusion and kinetic reactions that depend on surface electronic structures and interfacial properties [13]. It is worthy to mention that the formation of heterointerfaces will reflect on the ionic/electronic transmission capability and focus on the transformations of the intrinsic features, including position of Fermi level, bandgap width, charge separation ability, and electronic contribution of band structures (Fig. 1b). Furthermore, inspired by p-n heterojunctions with spontaneous built-in electric field effects to facilitate charge transport [14,15], it enables collective motion of electrons flowing through electrical contact layers into external circuits.

According to the binding mode and formation mechanism, the mixed-dimensional heterostructures (MDHs) can be classified into covalent and van der Waals (vdW) heteroepitaxy. In general, covalent heterostructures of two inorganic materials are connected by unoccupied bonds, termed as dangling bonds, on the surface of inorganic subtract in Fig. 1c. The covalent heterostructures will be formed through the “adatom–nucleation–growth” mechanism, wrapping the active substrate and establishing an inorganic capping layer through covalent bonds to reduce surface energy [16]. Owing to the strong binding energy of covalent bonds, even a small lattice mismatch can induce extended crystal defects and dislocations at the heterointerface, thereby acting as electron/ion leakage paths and further deteriorating the electrochemical performance of energy storage. Only a limited combination of two specific inorganic materials with similar lattice parameters can yield high-quality heterostructures because the angle and length of

the covalent bonds are difficult to alter. If we want to fabricate covalent heterostructures, the amount of strain in the film must be considered and determined by the lattice mismatch ε . If ε is greater than 9%, the heterostructure will experience a large volumetric strain when built with another inorganic layer [17]. Therefore, the covalent heteroepitaxy requires same lattice constants and intrinsic properties of materials. It is well known that two-dimensional

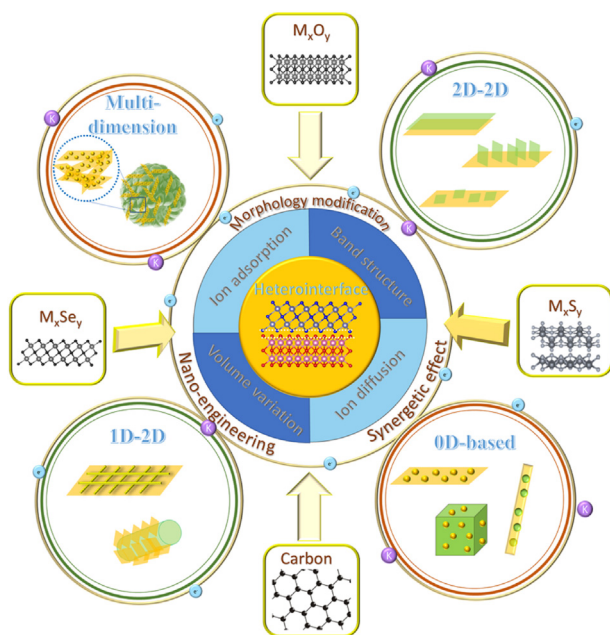


Fig. 2. Schematic illustration of the functional roles and structural design of mixed-dimensional heterostructures in potassium-ion storages.

materials (e.g. sheet, plate, flake) have great potential as a substrate, however, the problems related to surface stability without dangling bonds make it difficult to deposit another inorganic material by conventional covalent epitaxy.

In contrast to the covalent heterostructure, the heterointerface stress caused by lattice misfit and dislocation can be adequately alleviated by the noncovalent gap. The vdW heterostructures typically formed by adhesion or assembly *via* weak interaction between capping layer precursors and a non-dangling bonded substrate, which are proposed by Koma et al. in the semiconductor field (Fig. 1d) [14]. Accordingly, due to the free choice of substrate and overlayer from various lattice-matching conditions, the vdW heterostructures are regarded as a promising avenue to integrate high-quality MDHs with arbitrary two different dimensional surfaces and highly incommensurate physical parameter system. Besides, the electric contact of heterojunction between semiconductor and conductor will form the Schottky or ohmic junction, which depends on their Fermi level and work function [18,19]. A Schottky junction is created when the Fermi level of n-type semiconductor is higher than that of the metal. Schottky junctions have been shown to significantly change electronic properties, driven by close contacts between coupled components associated with strong built-in electric fields caused by large energy bandgap differences, resulting in remarkable rate capability [15].

In the past five years, although the design strategies and investigation of heterostructures have been carried out to address the challenges and bottleneck of electrochemical performances in LIBs and SIBs, the overviews of MDHs based on metal chalcogenides, metal oxides, and carbon for potassium-ion storages is lacking and in great request. Recently, Y. Dong et al. displayed the detailed electrochemical performance of 2D-based heterostructure. We here summarize the additional branch about the structural characterization and the technique and direction of simulation. In addition to the 2D materials, the construction and advantages of 0D, 1D, and 3D structures are also introduced into this minireview.

This minireview will focus on the fundamental understanding of formation mechanisms and corresponding electrochemical advancements and achievement of MDHs, as shown in Fig. 2, accompanied by state-of-the-art fabrication strategies and characterization techniques. Different MDHs of reported studies are detailedly summarized and generalized with various properties and

strengths of unique heterointerfaces. Moreover, we propose the current challenges and future perspectives on heterostructure anodes for next-generation alkaline-metal batteries.

2. Characterization of mixed-dimensional heterostructures

The formation and existence of heterojunctions or heterointerfaces must be demonstrated and confirmed using some characterization methods and instruments before discussing their synthesis and properties. Electron microscopy is a straightforward method to observe and identify morphologies and crystallographic planes, indicating preferred growth directions and plausible contact planes. Due to the environmental and spatial variation of molecular configurations, different vibration modes of single-phase materials and heterostructures can be detected by Raman spectroscopy. Furthermore, the covalent heteroepitaxy can be measured through the emission and absorption spectroscopy, which probes the chemical states and valances, respectively. With the complete materials and structure characterization, the subsequent DFT calculation and electrochemical testing of MDHs can be more credible in results and scientific knowledges. Therefore, we will detailly introduce the corresponding characterization methods applicable to inorganic heterostructures (Fig. 3).

Scanning electron microscopy (SEM) is a common electron microscope used to observe topography. The preliminary dimensionality and size of heterostructures can be determined in both cross-sectional [20] and plan-views [21]. Moreover, the field-emission SEM has been used to study several multilayer heterostructures in the semiconductor industry [22]. On the basis of the transmission electron microscopy (TEM) observations, we can simultaneously notice the morphology evolution and lattice spacing of heterointerface. High-resolution TEM (HRTEM) images clearly indicated an intimate and continuous interface with a heterojunction, confirming that the proper interface match is formed when two or more materials are assembled into the MDHs [23–25]. However, the clear superlattice structure formed between two identically oriented lattices cannot be visualized by SEM images. Thus, the HAADF-STEM is used to confirm the types of binding mode, whether there exists the vdW gaps or covalent bonds between the two materials. Both lateral and vertical epitaxy of heterostructures can be demonstrated by the planar view and cross-

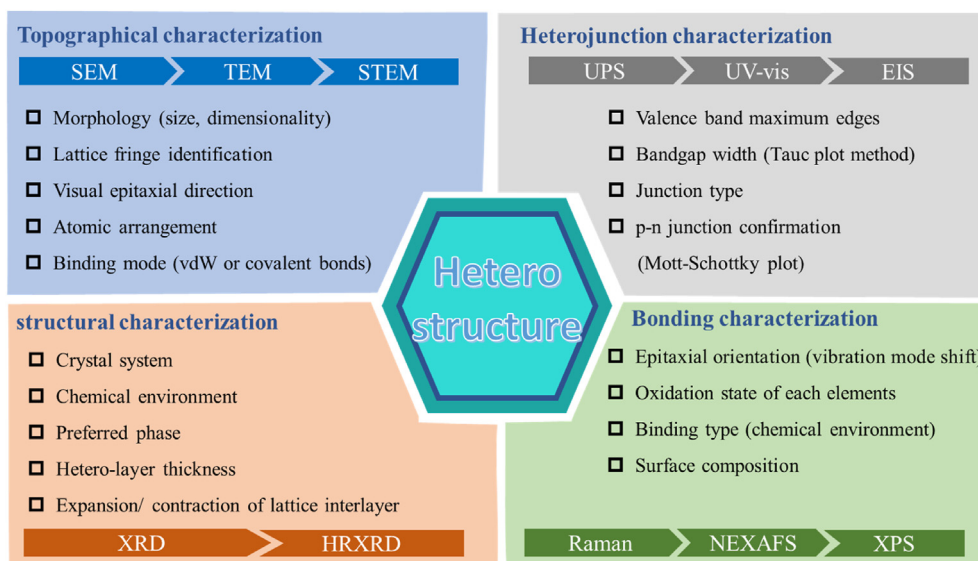


Fig. 3. Summary of characterization techniques and methods for heterostructures.

sectional STEM studies. Li et al. showed a high resemblance but in fact highly distinct atomic stacking orders for the high-resolution STEM image of 2D vdW heterostructure, suggesting a nearly ideal vdW interface across the vertical heterojunction between metallic and semiconducting transition-metal dichalcogenides (TMDs) [26]. These planar-view TEM and STEM studies and analyses confirm a fully oriented vdW epitaxy relationship, which also can measure the width of vdW gap [27]. Even covalent heterojunction of lateral materials can be revealed by the high-resolution STEM image; moreover, their interface is distinguishable because of the distinct atomic numbers of the two materials such as WS₂ and MoS₂ [28].

The bandgap of semiconductor in heterostructure plays a significant role for electric properties, which can influence the charge transfer between two materials. The ultraviolet photoelectron spectroscopy (UPS) can perform to investigate the electron band configuration [29]. The valence band maximum edges for each material in heterostructure can be measured. Because of the different positions of Fermi level between p-type and n-type semiconductors, the spontaneous electron transfer occurs during the formation of p-n junction, leading to a built-in electric field. According to Tauc plot method and ultraviolet-visible spectroscopy (UV-vis) [30], the bandgap can be determined by plotting square root of the absorption coefficient (α) and photon energy ($E = h\nu$) with photon energy, demonstrating that a section of straight line with the curve and the x-intercept of this line gives the optical bandgap. For example, Li et al. exhibited the interfacial built-in electric field between p-type Co₃O₄ and n-type TiO₂, leading to the directional migration of polysulfides [15]. Yin et al. introduced a gradient energy band and a built-in electric field to facilitate spontaneous electron and AlCl₄⁻ anion transfer [14]. Besides, the Mott-Schottky plot describes the reciprocal of the square of capacitance versus the potential difference between bulk semiconductor and bulk electrolyte through electrochemical impedance spectroscopy (EIS) [31]. The coexistence of the positive and negative slopes determines the successful construction of p-n junction characteristic [32].

Since near-edge X-ray absorption fine structure (NEXAFS) spectra are very sensitive to the local chemical environment and element specificity, it has been proved to be useful tools for studying heterostructured interactions. Understanding the interfacial charge transport mechanism of heterostructures is crucial for building high-performance energy storage systems [33]. NEXAFS is used for different kinds of heterostructure to understand the molecular orientation and binding mechanism [34,35], and it shows electronic transitions from a core initial state to an absorbing edge with well-defined symmetry to an unoccupied valence state [36]. For example, the signal shift in MoN-VN to a higher energy implies a higher oxidation state of Mo in MoN-VN compared with peak positions of MoN, originating from a reduced electron density of Mo in heterostructure due to the strong coupling between two materials [37]. Furthermore, the Raman spectroscopy also can be used to reveal the possible epitaxial direction of heterostructures. There are two main Raman-active peaks, the in-plane and out-of-plane mode, the former red-shift while the latter blue-shift with the increase of layer number. Compared with original peaks of pure materials, the frequency difference of heterostructures can confirm the number of layers, even heterogeneous layers [38]. For instance, Raman scattering of heterostructures has been examined by Liang et al. to determine that their spectra can be used to identify stoichiometric and stacking modes [39]. The red-shift of E¹_{2g}-Mo of monolayer MoS₂ and WS₂ is attributed to increased dielectric shielding to the Mo layer in the presence of the W layer. Obviously, the environmental change may cause some variation between their Raman spectra [40,41].

X-ray photoelectron spectroscopy (XPS) is used to elucidate electronic structure and elemental composition, and to probe the chemical bonding information and oxidation state of the samples on the surface [42]. Strong chemical interactions between heterostructure and polysulfide are also manifested and analyzed [43]. XPS can further detect that an element on one material is connected to another element on another material if a covalent bond is formed within the heterointerface. Ma et al. confirm the existence of a chemical bond between Mo(S, Se) and C using the XPS spectrum, indicating the formation of heterostructures [44]. In addition to the analysis of surface composition, the X-ray diffraction (XRD) can detect the existence of at least two materials with their characteristic diffraction peaks. Most importantly, the hetero-layer thickness and composition within the heterostructure can be qualitatively confirmed by High-resolution XRD, which can more precise the crystal spacing from the ideal crystal structure [45,46]. Lattice expansion and contraction of the interlayer in heterostructure also can utilize to probe the single-crystalline distribution [47].

3. The roles and significance for heterostructures in potassium-ion storages through theoretical simulation

In addition to the aforementioned tools for proving the existence of heterointerfaces, the types of heterostructures and their features have been estimated and explained by density functional theory (DFT). DFT can predict the possibility of heterostructure formation in the interface and the different ion transport/adsorption capabilities of the pristine material and the heterostructure. First, we can model the crystal structure by measuring the crystal system and crystal plane of the heterostructure from the results of the XRD pattern and HR-TEM image. Second, the compatibility of two materials will be verified by suitable surface energy for specific crystalline plane and connection angle. Fundamental properties of heterostructure, including density of state and charge density difference, can be clearly simulated. Third, the adsorption site and pathways with smallest relative energy are simulated and calculated to show advantages consistent with the electrochemical performance and analysis. The corresponding advantages and simulations of heterostructures in PIBs are listed below.

3.1. Promoting adsorption of potassium ions or polysulfides

Numerous reported studies have calculated and demonstrated theoretical simulations of K ion adsorption energies for heterostructures [44,48–50]. However, conversion-type materials dominated by metal sulfides and selenides lead to a severe loss of potassium-state high-capacity-contributing intermediates. In addition to potassium-sulfur or potassium-selenium batteries [51,52], some metal chalcogenide or TMDs anode, the potassium polysulfides or polyselenides in PIBs will dissolve into electrolyte, and even transfer to another electrode, called shuttle effect, resulting in the loss of active substances and shortening the lifespan. Cao et al. proposed that VS₄ with an unsaturated bridge (S₂)²⁻ could serve as an anchoring site to stabilize the intermediate K_xS_y with an efficient entrapment effect [53]. Also, the heterostructure can maintain layered SnS and tune the distribution of K_xS_y with high conversion reversibility. The (111) plane of SnS and VS₄/SnS heterostructure have been selected and constructed to adsorb K₂S (Fig. 4a). The data showed that the VS₄/SnS@C heterostructure exhibited stronger adsorption of K_xS_y than SnS@C (Fig. 4b). Furthermore, adsorption experiments were performed by dispersing sufficient SnS@C and VS₄/SnS@C in the electrolyte containing K₂S chemical (Fig. 4c). It is clearly demonstrated that the K₂S electrolyte with the heterostructured composite changed from

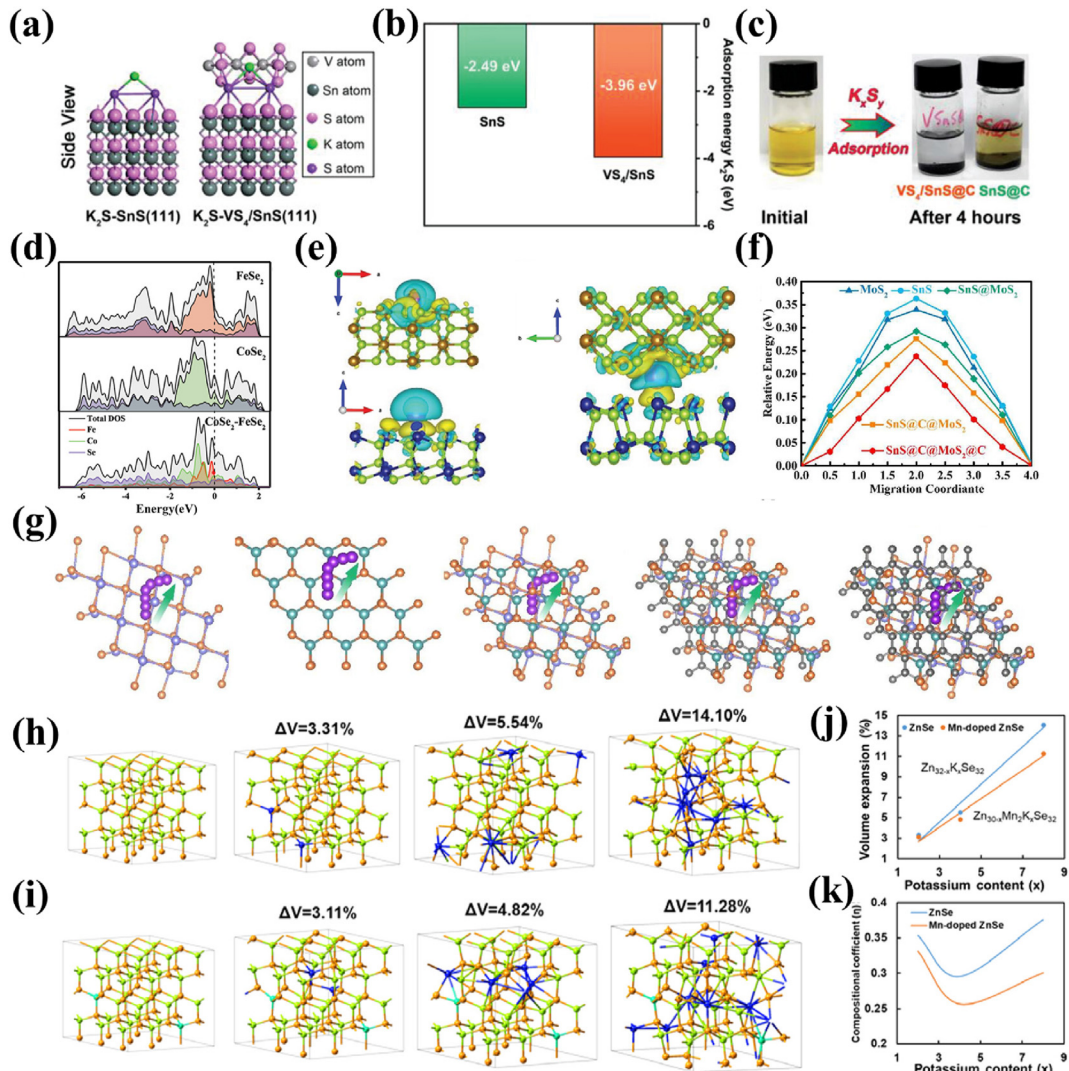


Fig. 4. (a) The most stable adsorption sites for SnS@C and VS₄/SnS@C with K₂S. (b) K₂S adsorption energy of VS₄/SnS@C and SnS@C. (c) The chemical adsorption experiment of K₂S in electrolyte. Reproduced with permission from Ref. [53]. Copyright 2021, John Wiley and Sons. (d) DOS analyses and (e) charge density difference for CoSe₂, FeSe₂@C, and CoSe₂/FeSe₂@C. Reproduced with permission from Ref. [49]. Copyright 2021, John Wiley and Sons. (f) the diffusion energy barrio and the corresponding K-ion migration path with top views of SnS, MoS₂, SnS@MoS₂, SnS@C@MoS₂, and SnS@C@MoS₂@C. Reproduced with permission from Ref. [71]. Copyright 2022, Elsevier. (h, i) Volume variation ratio of ZnSe and Mn-doped ZnSe during K-ion insertion. (j, k) Percentage volume expansion per degree and compositional expansion coefficient of potassium in ZnSe and Mn-doped ZnSe. Reproduced with permission from Ref. [72]. Copyright 2021, American Chemical Society.

yellow to colorless, indicating that the VS₄/SnS @C composite has a strong adsorption effect on K₂S and there is an effective entrapment effect of VS₄/SnS. Moreover, Chen et al. demonstrated that KFeS₂/graphene has a strong adsorption capability for K₂S, K₂S₂, K₂S₃, K₂S₄, and K₂S₅, and the existence of the interface between KFeS₂ and graphene can boost the K-ion mobility [54]. The corresponding advantage of capturing polysulfides enhanced the long-term cyclability of conversion anode, with Columbic efficiency approaching 100%. Jayan et al. calculated the projected density of states and Gibbs free energy of each elementary sulfur reduction reaction, unraveling that the retained metallic character of VS₂ after polysulfides adsorption and a significant decrement in energy barrier due to the catalytic activity of the VS₂ surface, respectively [55]. The CoNiO₂/Co₄N heterostructure is indicated as a higher binding energy, implying tighter anchoring ability and rapid adsorption compared to individual CoNiO₂ and Co₄N [56].

3.2. Facilitating charge transfer capability and ionic/electronic conductivity

Due to the influence and variation of different features and dimensionality of heterostructures, theoretical simulations can be performed to verify the existence of the built-in electric field. The first principle DFT calculation determines the existence of an internal electric field in the band structure of heterointerface via charge density differences and density of states (DOS). We focus on the DOS intensity near the Fermi level and the gap between the valence and conduction bands. Additionally, the “differential” refers to the redistribution of charges when atoms form clusters or the chemical composition or geometric configuration of the system is changed [57]. Thus, it can be seen intuitively the bonding or the distribution condition of the individual atoms in the system through different diagrams. The polarity of the bond is determined

by the specific spatial distribution of charge accumulation/depletion, and the orbital of the bond is dependent on the shape of the charge distribution near a grid point, mainly the analysis of the d-orbital. As shown in Fig. 4d, Shan et al. found that CoSe₂/FeSe₂@C heterostructure exhibited lower overpotentials than CoSe₂ and FeSe₂, indicating an effective K-ion diffusion and fast electron transfer. To further examine the heterojunction effect, there is a narrow bandgap in FeSe₂ and when the heterojunction structure is achieved, the bandgap is shifted near the Fermi level, which means that the conductivity is optimized compared to pure FeSe₂ and CoSe₂. As shown in Fig. 4e, a significant charge transfer from CoSe₂ to FeSe₂ is observed, further confirming the unbalanced charge distribution in the calculated results [49]. In order to gain insight into the benefits of heterostructures on electrochemical performance, many studies have been carried out on heterostructures in PIBs to elaborate and analyze DOS and charge density difference diagram (e.g. analysis of electric conductivity or electron transfer [50,58], ionic interaction [48,59], bonding condition [60,61]).

3.3. Providing fast ion diffusion channels with low energy barrier

The diffusion behavior and performance can be displayed by electrochemical analysis, such as galvanostatic intermittent titration technique (GITT) [62,63], Randles–Sevcik method [64–66], or EIS [12,67]. We also can use the DFT calculation to predict or confirm the electrochemical performances. First, the modules will follow the lowest energy barrier of adsorption site to simulate the

continuous diffusion path [44]. It is also possible to calculate the different crystalline phases of the diffusion pathways and find the easiest way for K ions to diffuse through the outer surfaces or interlayers of the material [68–70]. The potassium-ion migration paths in SnS, MoS₂, SnS@MoS₂, SnS@C@MoS₂, and SnS@C@MoS₂@C heterostructures are shown in Fig. 4g, along with the corresponding K migration energy barriers along the diffusion paths are also plotted in Fig. 5f. Apparently, the K-ion diffusion barrier at each site in the SnS@C@MoS₂@C composite is the smallest among all preparation models, confirming the fast ionic transportation of K⁺ ions [71].

3.4. Restricting volume variation

The volume variation of active materials is one of the critical problems in PIBs with insertion of larger K ions. The instability of large ionic radius of K ions during the potassiation-depotassiation process is one of the main reasons for the dramatic volume change of metal chalcogenides, resulting in structural cracking, increased charge transfer resistance, and shortened shelf life. According to the simulation of the atomic configuration, we can calculate the lattice volume expansion as a stepwise insertion of K ions. Liang et al. purposed the heterogenous Mn-doped ZnSe and demonstrated the volume expansion crystal structures of pure and Mn-doped ZnSe with different content of K ions during potassiation process given in Fig. 4h and i [72]. The lattice constants were determined by geometric optimization of the crystal structures of

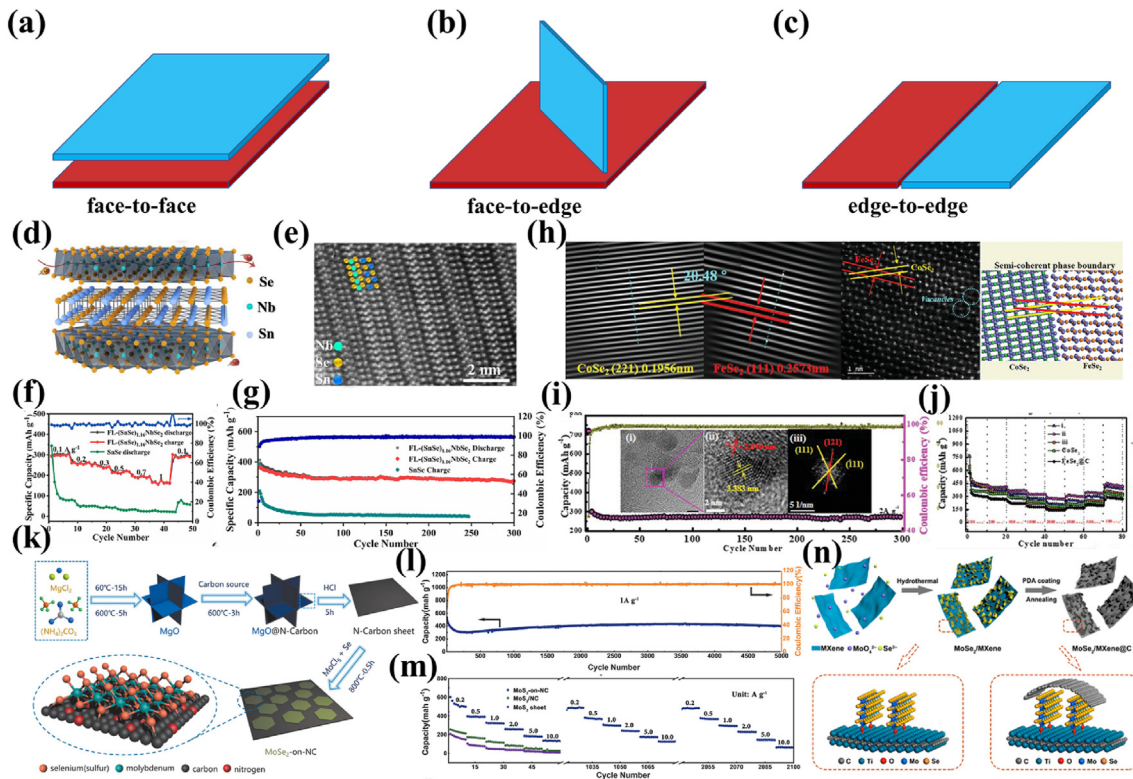


Fig. 5. Schematic diagrams of 2D-2D heterostructure in PIB constructed through (a) face-to-face, (b) face-to-edge and (c) edge-to-edge stacking direction. (d, e) Schematic diagram and HRTEM and HAADF-STEM images of (SnSe)_{1.16}NbSe₂. (f) Rate capabilities and (g) long-term cycling performance of SnSe and FL-(SnSe)_{1.16}NbSe₂. Reproduced with permission from Ref. [74]. Copyright 2021, Elsevier. (h) The inverse fast Fourier transformations, HAADF-STEM image, and the corresponding schematic diagram of CoSe₂/FeSe₂@C. (i) Cycling stability at 2 A/g of the CoSe₂/FeSe₂@C; the insets are TEM images and the corresponding FFT pattern. (j) rate performance of all the samples. Reproduced with permission from Ref. [49]. Copyright 2021, John Wiley and Sons. (k) Schematic illustration of synthesis of 3D hierarchical heterostructures and the microscopic sketch of the heterostructures construct by MoS₂ and carbon sheet. (l) Comparison of ultralong cycle performance of MoS₂-on-NC at 1 A/g. (m) Comparison of rate cycle performance of MoS₂-on-NC, MoS₂/NC, and MoS₂ nanosheet at various current density. Reproduced with permission from Ref. [44]. Copyright 2020, John Wiley and Sons. (n) Schematic of the preparation of MoSe₂/MXene@C. Reproduced with permission from Ref. [80]. Copyright 2019, American Chemical Society.

ZnSe and Mn-doped ZnSe and used as the percent volume change during potassiation. The volume expansion of Mn-doped ZnSe was lower than that of ZnSe, meaning that positive influence of heterointerface on the structural stability of most TMDs and metal chalcogenides. It is an important technique to confirm the Columbic efficiency and durability of the SEI layer. The compositional expansion coefficients (η) were calculated to illustrate the variation law of volume expansion of ZnSe and Mn-doped ZnSe. The η was calculated and as a function of α and V_i and V_f , where α is concentration of K ions and the volume results from DFT calculation before and after the addition of K ions [73]. As shown in Fig. 4j and k, the η of Mn-doped ZnSe is similar to that of ZnSe at initial stage. The η of ZnSe increases significantly after K-ion insertion because the structure of pure ZnSe is damaged with the increase of K atoms. Accordingly, the mechanical strength of heterogeneous Mn-doped ZnSe is enhanced owing to the Mn-induced electronic structure of ZnSe.

4. Design strategies and electrochemical evolution of mixed-dimensional heterostructures

The construction and modification of heterointerfaces of mixed-dimensional M_xS_y , M_xSe_y , M_xO_y (M = metal or transition metal) and carbon materials are important to ensure higher cycle life and satisfactory energy density. Rational design of anodes can enhance the structure stability and increase specific capacity. Here, we mainly discuss four different mixed-dimensional heterostructure geometries, namely 2D–2D, 1D–2D, 0D, and MDHs. In addition, we list a large number of literature whose rate capability and cycling capability in Table 1, and the corresponding material designs and advantages will be introduced and reviewed in detail in the following sections.

4.1. 2D–2D heterostructures

Due to its high theoretical capacity and large interlayer spacing, 2D TMDs have become attractive anode materials for PIBs. There are three connection types of heteroepitaxial, face-to-face, face-to-edge, and edge-to-edge heterostructures, as shown in Fig. 5a–c. The structural features and connection types depend on the lattice parameters and crystal structure. Peng et al. designed the face-to-face structure of misfit layered compounds (MLCs) by a facile solid sintering method (Fig. 5d and e). Combining the high conductivity of NbSe₂ and the high reactivity of SnSe₂, this novel heterostructure exhibits high-strength flakes and weak interlayer adhesion. The significantly improved rate performance of NbSe₂-based MLCs is shown in Fig. 5f, and their high Coulombic efficiencies at various current densities and excellent stability with current rate increased perform the great reversibility of the face-to-face heterostructure after 300 cycles (Fig. 5g) [74]. Because carbon-based conductors can be also used as two-dimensional template and active material, the utilization of 2D-based carbons with semiconductors that can form heterojunctions associated with Schottky contacts has been proposed, such as Bi_{0.51}Sb_{0.49}OCl/rGO [75], SnS₂/Ti₃C₂T_x [76], C/MoS₂/G [77]. Ma et al. assigned a chemical vapor deposition (CVD) process for fabricating the ultrathin MoSe₂ nanosheets uniformly distributed on the hollow carbon nanosheets, as shown in Fig. 5k. The XPS spectrum shows the C1s and Mo 3 d of MoS₂-on-NC, and the peaks located at 286.2 eV and 283.1 eV can be attributed to the formation of covalent C–Se and C–Mo bonds, respectively [44]. Chemical bonds can enhance the mechanical stability of nanosheets and improve the structural integrity of electrode materials after repeated charge and discharge. Therefore, the outstanding performances of MoS₂-on-NC

heterostructure have displayed the ultrastable cyclability and rate capability with current density of 1 A/g and 10 A/g (Fig. 5l and m).

In-plane CoSe₂–FeSe₂ heterostructure is formed with semi-coherent phase boundary, which is stitched together at the edge [49]. The high angle annular dark-field STEM (HAADF–STEM) technique and structure scheme were displayed to visualize the evolution of the heterointerface in Fig. 5h. Structural features can suggest that the atomic arrangement in the edge-to-edge CoSe₂/FeSe₂ heterointerface is slightly disordered. The great cycling performance and structural durability of CoSe₂/FeSe₂ after cycling processes are shown in Fig. 5i and its inset. Thanks to the lower energy barriers of ion migration when passing through multiphase transitions, the superior rate capability of CoSe₂/FeSe₂@C performed a considerable reversible capacity at step current densities, as shown in Fig. 5j. Compared with SnS@C, Cao et al. proposed a hierarchical VS₄/SnS heterostructure with 2D–2D nanosheet morphology anchored to a wrinkled graphene framework. In comparison, the charge transfer resistance (R_{ct}) of VS₄/SnS before cycling was smaller than that of SnS@C, suggesting a superior kinetic reaction of layered VS₄/SnS heterostructure. Particularly, VS₄/SnS exhibits a lower overpotential and higher K ion diffusion coefficient than SnS, suggesting that the heterointerface between VS₄ and SnS may contribute to the K-ion diffusion [53]. A face-to-edge heterostructure, however, has not been published in PIBs or PIHCs system. In recent, there are some reported literature used this concept to fabricate the heterostructure applied on other systems. Yu et al. designed a heterostructured composite with ZnS nanosheets and carbon coating Cu₂S nanoplates in sodium-ion battery [78]. A unique vertical 2D/2D SnS/SnS₂ heterostructure grown on the surface of rGO was reported by Huang et al. [79]. MoSe₂ nanosheets were vertically grown on the surface of MXene flakes through the hydrothermal method, resulting in the MoSe₂/MXene hybrid nanosheets, as shown in Fig. 5n. The MoSe₂ nanosheets were anchored to the MXene flakes via strong covalent bonds, which significantly improves the stability of the hybrid structure and facilitates the transfer kinetics of ions and electrons during electrochemical reaction [80].

4.2. 1D–2D heterostructures

One-dimensional (1D) nanomaterials (*i.e.* nanowires, nanorods, nanoribbons, nanotubes, etc.) have received much attention as promising materials with outstanding electronic properties [81] due to several important structural advantages over conventional planar materials: High surface area-to-volume ratio for enlarged active layer area [82]; high-quality heteroepitaxy on highly lattice-mismatched substrates without distortion [83]; and structural versatility in designing heterostructures through radial or axial compositional modulation [16,84]. These merits of 1D nanomaterials greatly increase the freedom in heterostructured engineering and enables a wide range of alloy compositions. Hence, the integration of semiconductor nanowires with 2D materials is expected to create unique features for potassium-ion storages. Due to their anisotropic geometry, 1D–2D heterostructures have more possible configurations, which can be divided into vertical and parallel stacking forms, the former mainly relying on covalent bonds and the latter mainly generated by vdW forces [85]. Vertical and surface stacked heterostructures are formed by the deposition of 2D nanosheets on 1D nanomaterials to form forests, and 1D nanomaterials are directly grown on the surface of 2D nanosheets to obtain arrays (Fig. 6a and b).

Cao et al. proposed a microbe-assisted assembly strategy to address the self-aggregation, large volume change, and rapid capacity decay of MXene-based materials in PIBs by forming a heterogeneous porous structure of 2D MXene on 1D fungal-derived

Table 1

List of mixed dimensional materials in PIB system.

Dimension	Materials	Strategies	Rate capability ^a	Cyclability ^b	Ref.
2D-2D	(SnSe) _{1.16} NbSe ₂	Solid sintering	300/0.1, 150/1	300/300/0.1	[74]
2D-2D	(PbSe) _{1.14} NbSe ₂		300/0.1, 175/1	250/260/0.1	
2D/2D	VS ₄ /SnS@C	1. Solvothermal 2. Sulfidation	270/0.1, 123/10	150/6000/1	[53]
2D/2D/2D	C/MoS ₂ /G	1. Oxidative polymerization 2. Sulfidation	362/0.1, 195/10	126/4000/5	[77]
2D/2D	Bi _{0.51} Sb _{0.49} OCl/rGO	NaBH ₄ reduction	407/0.1, 319/1	360/1000/0.1	[75]
2D/2D	MoS ₂ -on-NC	one-step CVD	498/0.2, 130/10	399/5000/1	[44]
2D/2D	MoSe ₂ -on-NC		393/0.2, 171/5	247/4800/1	
2D/1D	MXene@NCRib	1. Freeze-drying 2. Annealing	371/0.1, 60/5	202/1000/1	[86]
1D/2D	CoTe ₂ /MXene	1. Hydrothermal 2. Tellurization	420/0.2, 128/20	232/3000/2	[88]
1D/2D	V ₂ O ₅ @rGO	Hydrothermal	265/0.03, 50/2.94	179/500/0.15	[87]
0D/1D	Fe ₂ VO ₄ NC	Solvothermal	389/0.1, 228/2	196/2300/4	[96]
0D/2D	FeS@SPC	1. Calcination 2. Sulfidation	388/0.1, 140/5	323/3000/1	[97]
0D/2D	MoS ₂ /Sb @C	1. Hydrothermal 2. Sulfidation	345/0.05, 235/2	170/1000/1	[98]
0D/3D	MoSe ₂ @MoO ₂	Hydrothermal	365/0.1, 172/2	255/100/0.5	[100]
2D/3D	VO ₂ -V ₂ O ₅ /NC	Self-template strategy	510/0.1, 108/10	256/1600/1	[110]
0D-2D-3D	Fe ₂ S ₈ C@d-MoS ₂	Hydrothermal	505/0.5, 318/5	280/500/4	[109]
1D-1D-2D	MnCo ₂ O _{4.5} @ MnCo ₂ S @rGO	two-step hydrothermal	357/0.1, 125/2	273/400/1	[104]
2D-2D/3D	MoS ₂ -WS ₂ -C	Spray pyrolysis	377/0.1, 176/5	350/100/0.2	[105]
0D-1D	Bi ₂ S ₃ /MoS ₂ @NC	Solvothermal	551/0.1, 381/5	412/400/0.5	[106]
0D-0D/3D	CoSe ₂ -Cu ₂ Se@NC	1. Solvothermal 2. Sol-gel 3. Selenidation	550/5, 460/25	367/2000/20 415/2000/10	[60]
0D-0D	CoS ₂ /CuCo ₂ S ₄ @NC	1. Solvothermal 2. Sol-gel 3. Calcination	563/0.2, 117/2	112/1000/1	[108]
0D-0D	CoSe ₂ -FeSe ₂ @C	1. Coprecipitation 2. Selenidation	407/0.1, 275/2	271/300/2	[49]
0D/0D	Sb@Sb ₂ O ₃	Spray pyrolysis	573/0.1, 302/30	379/10,000/5	[61]
2D-2D	SnS ₂ /SnO ₂ /stainless steel mesh	Hydrothermal	470/0.05, 150/1	155/250/0.5	[91]
0D-2D-3D	Co ₉ S ₈ /NSC@MoS ₂ @NSC	1. Calcination 2. hydrothermal	414/0.1, 163/2	141/800/3	[107]
2D-2D/3D	SnS@C@MoS ₂ @NC	1. hot injection 2. hydrothermal 3. Calcination	566/0.05, 305/1	253/3000/1	[71]
Hetero-phase boundary/3D	CS-Se@NC	1. Coprecipitation 2. Carbonization 3. Selenidation	368/0.1, 183/2	105/200/0.5	[103]

^a The rate capability is summarized as capacity/current density. The unit of capacity and current density are mA h/g and A/g, respectively. b) The cycling performances are summarized as capacity (mAh/g)/cycle number (cycles)/current density (A/g).

nitrogen-rich carbon nanofibers (Fig. 6d) [86]. With surface-controlled storage of large K ions of 2D MXene and charges transportation of inner conductive 1D NCRib network, the superior potassium-ion storage performances were enhanced by improving ionic conductivity and surface pseudocapacitive contribution, as shown in Fig. 6e, which is consistent with the high-rate performance in Fig. 6f. When 1D nanomaterials are stacked around the surface of 2D materials, this designed heterostructure not only enhances reaction kinetics but also provides a more reactive surface area for potassium-ion storages [87,88]. Xu et al. prepared CoF(OH)/MXene by a one-step hydrothermal reaction and tellurization in the presence of MXene (Fig. 6g). Afterward, the transformation of CoTe₂ nanorods from hexagonal to orthorhombic phase was induced by phosphorus doping, resulting in the formation of 1D nanorods on 2D MXene, as shown in the TEM and HRTEM images in Fig. 6h [88]. With the construction of crystal structure and DFT calculation (Fig. 6i and j), the K-ion diffusion barrier of o-P-CoTe₂/MXene was lower than those of h-CoTe₂/MXene, h-CoTe₂, and MXene anodes. Hence, the capacitive contribution of o-P-CoTe₂/MXene was as high as around 90% at the scan rate of 1.1 mV/s, larger than those of other materials for the surface-controlled potassium storage in Fig. 6k. The rate capability of

o-P-CoTe₂/MXene also delivered the reversible capacities of 420 and 168 mAh/g at 0.2 and 20 A/g presented in Fig. 6l, respectively. Numerous similar heterostructures have been successfully fabricated, including WVO₄/V₃Se₄ [89], V₂O₅@rGO [87], TMC@MXene@NCRib [90], SnS₂/SnO₂ [91], MoSe₂-G-CNTs [92]. Moreover, if the size of 2D materials is much larger than that of the 1D nanomaterial, the 1D nanostructures can vertically align the template of the 2D structures illustrated in Fig. 6c. This nanostructure can also achieve high specific surface area by inhibiting the self-aggregation of nanomaterials. The vertically aligned 1D Te nanowire-2D Sb₂Te₃ nanoblades heterostructure fabricated via solvothermal method by Yin et al. gives the rational guidance to design cooling-fins-like nanostructures integrating 1D and 2D heterostructures for advanced anode materials with extraordinary rate performance [93]. The vertically aligned Te nanowires can bridge adjacent Sb₂Te₃ nanosheets to form 3D layered structures with tunable porosity and enhanced electron transport paths.

4.3. Zero-dimensional-based (0D) heterostructures

In general, the 0D nanomaterials (e.g. nanodots, nanoparticles, nanospheres, etc.) can provide the following advantages. First, the

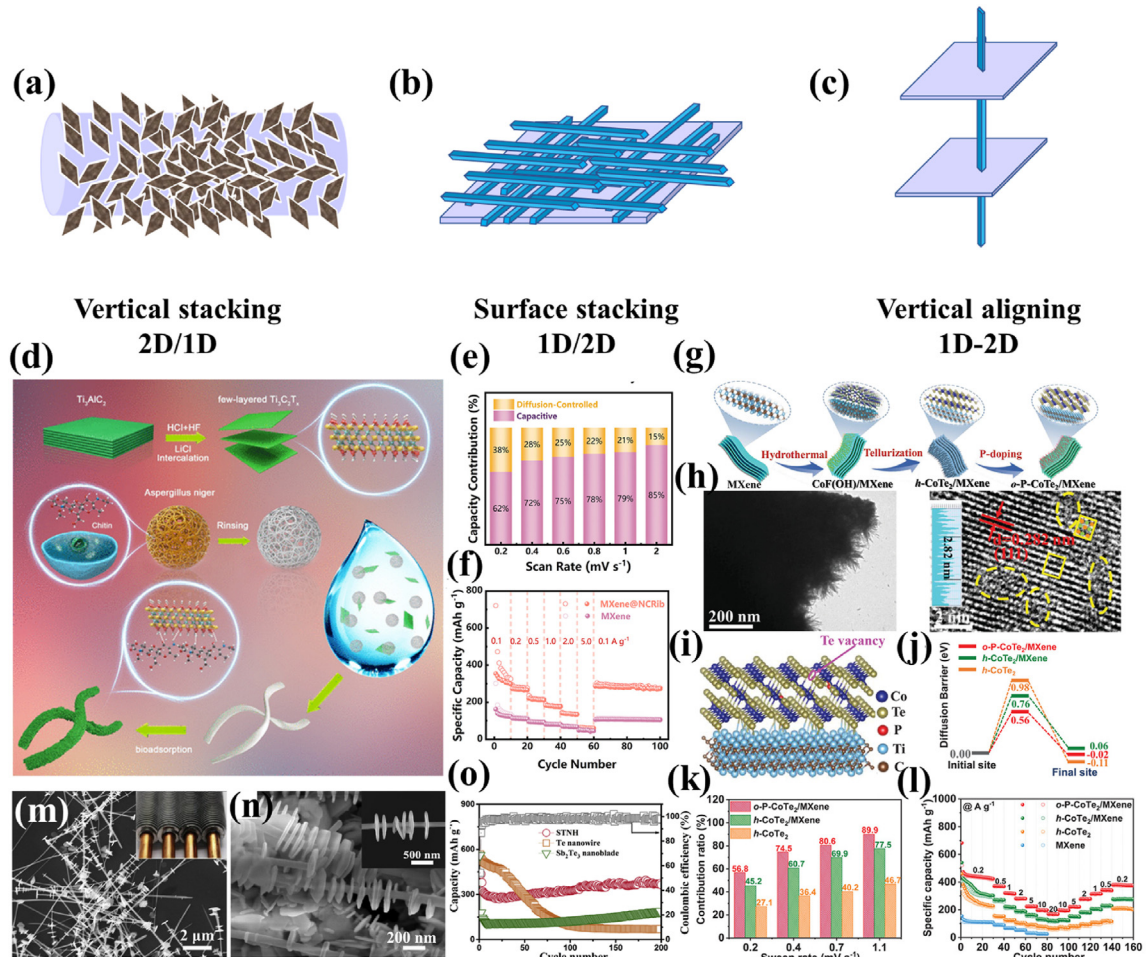


Fig. 6. Schematic diagrams of 1D-2D heterostructure constructed through (a) vertical stacking, (b) surface stacking, and (c) vertical aligning direction. (d) Schematic Illustration of Microbe-Assisted Assembly of 2D/1D MXene@NCRib. (e) Capacity contribution ratio at different scan rates. (f) Rate capability of the MXene and MXene@NCRib. Reproduced with permission from Ref. [86]. Copyright 2021, American Chemical Society. (g) Schematic illustration of the preparation process of o-P-CoTe₂/MXene. (h) TEM and HRTEM image of o-P-CoTe₂/MXene. (i) Side view of the crystal structure of o-P-CoTe₂/MXene interface. (j) Energy barriers for K diffusion in o-P-CoTe₂/MXene, h-CoTe₂/MXene, and h-CoTe₂. (k) The contribution ratio of capacitive behaviors at different sweep rates for o-P-CoTe₂/MXene, h-CoTe₂/MXene, and h-CoTe₂. (l) Rate capability of o-P-CoTe₂/MXene and other electrodes. Reproduced with permission from Ref. [88]. Copyright 2021, John Wiley and Sons. (m, n) SEM images of the STNH under different magnifications and the inserts are cooling-fins-like 1D Te - 2D Sb₂Te₃ heterostructure and high-resolution SEM, respectively. (o) Cycling performance of STNH electrode at a current density of 100 mA/g. Reproduced with permission from Ref. [93]. Copyright 2020, Elsevier.

uniformly dispersed nanoparticles with high electrolyte-electrode contact area are ideally proper for conducting infiltration of electrolyte and electrochemical reaction of active materials [94]. Second, nanoparticles can shorten ion/electron diffusion distance, and migrate strain induced by volume change owing to the surface effect and small size effect [95]. Nevertheless, the severe aggregation of 0D nanomaterials due to their high surface energy would lead to poor cyclability and rate capability. Thus, engineering design of heterojunction combined with other dimensional materials is an imminent demand.

The 0D-based heterostructure anode can be classified into 0D–1D, 0D–2D and 0D–3D heterostructures, as illustrated in Fig. 7a–c. Yang's group adopted a one-pot synthesis to fabricate the heterostructures composed of 0D Fe₂VO₄ nanobead encapsulated in 1D N-doped carbon nanowires (Fig. 7d and e). The inner void space and outer carbon shell effectively prevent the aggregation of active materials and promote electronic and fast transport of ions and adapt to volume changes during cycling [96]. Even after charging/discharging process, the R_{ct} of heterostructure was reduced and smaller than that of pristine material, which means that the structure can be maintained without cracking. Based on

the unique structure, the rate capability and cycling durability of the heterostructure are improved, with a high capacity of 196 mAh/g after 2300 cycles at 4 A/g in Fig. 7f. Design of heterostructures of 0D FeS nanodots were embedded in 2D sulfur-doped carbon nanosheets (Fig. 7g), as reported by Yan et al. [97], and the junction-enhanced adsorption of K ions was improved. After cycling test, the post-mortem TEM images showed the entire wrapped heterostructure without exposition and rupture of active materials in Fig. 7h. Particularly, there are many reported studies that adopted the design concept of 0D-2D heterostructures. The Chrysanthemum-like heterostructures were constructed by encapsulated Sb nanoparticles into the few-layered MoS₂ nanosheets, which were further impregnated into the N-doped graphene [98]. Benefiting from the synergistic coupling effect between the outer graphene and inner MoS₂/Sb heterostructure, the electron transport, and ion diffusion were effectively accelerated. Furthermore, introducing 0D nanomaterials into 3D framework can further enhance the structural durability and interlinked porous channels with engineering the heterojunction [99]. Jiang et al. designed a heterojunction of 0D MoO₂ nanoparticles confined in 3D MoSe₂ hollow sphere (M@M) prepared by hydrothermal synthesis

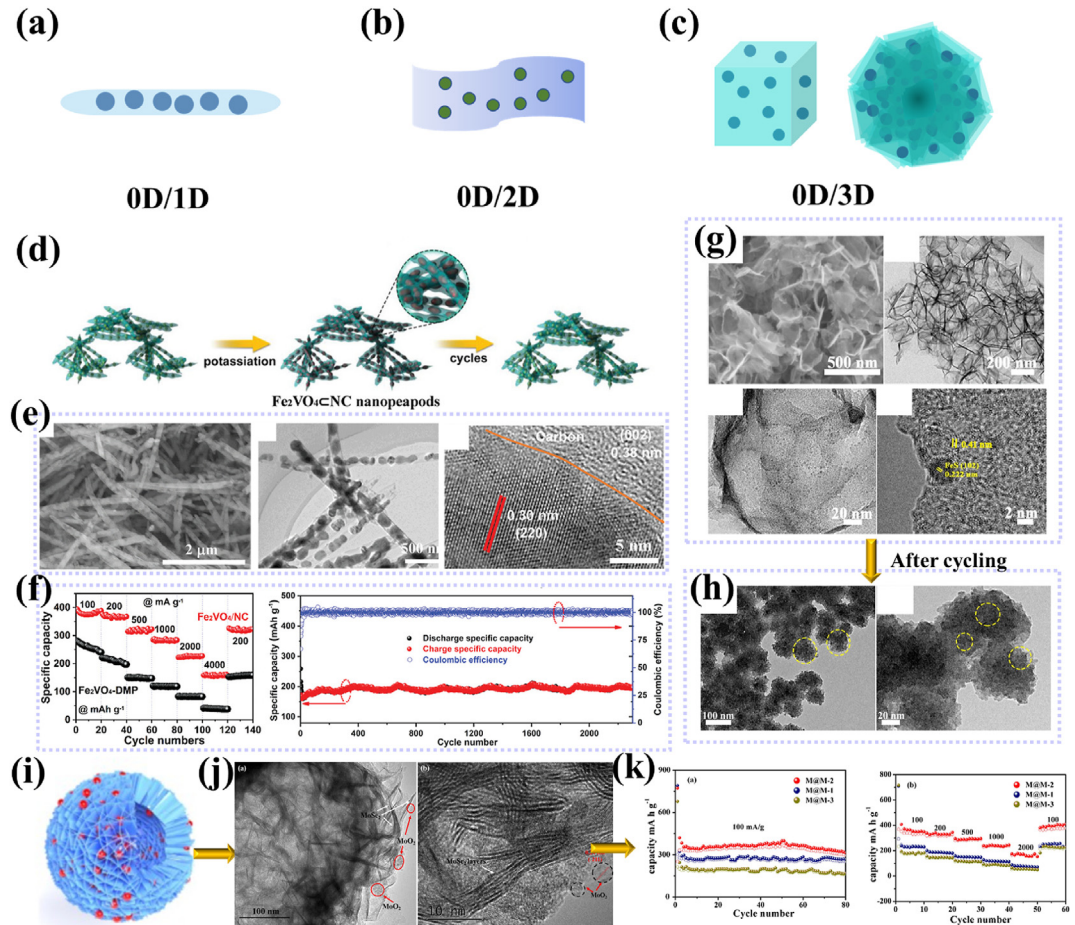


Fig. 7. Schematic diagrams of 0D-based heterostructures combined 0D nanomaterials with (a) 1D, (b) 2D and (c) 3D structures. (d) Schematic illustration of the preparation process. (e) SEM images, TEM images, and HRTEM images of the Fe₂VO₄-NC nano-peapods. (f) Rate capabilities and cycling performance of the Fe₂VO₄-NC nano-peapods at various current densities. Reproduced with permission from Ref. [96]. Copyright 2019, John Wiley and Sons. (g) Low-magnification and high-magnification TEM images of FeS@SPC. (h) Post-mortem TEM images of FeS@SPC after 3,000 cycles at 1A/g. Reproduced with permission from Ref. [97]. Copyright 2021, Elsevier. (i) Schematic illustration of preparation process of M@M samples. (j) TEM images and HRTEM images of M@M. (k) Cycle and rate performances of M@M samples. Reproduced with permission from Ref. [100]. Copyright 2020, Elsevier.

(Fig. 7i) with its built-in electric field facilitated the diffusion of K ions. The TEM image further showed that the MoO₂ nanoparticles are tightly connected to MoSe₂, as presented in Fig. 7j. As a result, the electrochemical performances of the heterojunction were effectively improved compared to the pure MoSe₂ and MoO₂ (Fig. 7k) [100]. Meanwhile, the layered double hydroxides shell with 3D network can prevent the aggregation of carbon dots during the ultralong cycle lifespan with promoting the electrical conductivity and stabilizing the electrode structure [101].

4.4. Multidimensional and other heterostructures

The combination of various dimensions of materials at the nano- or micro-scale achieves characteristic synergistic effects, where each individual component exerts its own strengths and overcomes the shortcomings of the other units. The rational integration of multidimensional nanoscale subunits combines multiple advantages, including enlarged electrode/electrolyte interface area, shortened electron/K ion diffusion paths, enhanced electrical conductivity, excitation of excellent pseudocapacitive behavior, inhibition of self-aggregation of nanoparticle, and accommodating volume variation of electrodes during the cycling process [102].

Due to the structural interconnectivities, MDHs not only possess well-developed channels for rapid electron transfer, but also offer a large specific surface area, and more active sites, which can enhance the electrochemical reactivity. Furthermore, several other configurations without specific morphology of heterostructures have been reported in PIBs, including CoSe₂/SnSe₂@NC [103], MnCo₂O_{4.5}@MnCo₂S₄@rGO [104], MoS₂-WS₂-C [105], and Bi₂S₃/MoS₂@NC [106].

Yang et al. designed a synthetic route to fabricate multidimensional composites in which 0D Co₉S₈ nanoparticles and 2D MoS₂ nanosheets were incorporated into a 3D N, S-doping carbon scaffold, as shown in Fig. 8a. The field emission SEM and TEM images of MDH displayed highly uniform nanoboxes encapsulated by crumpled MoS₂@C nanosheets and a shell thickness and inner cavity size of 175 and 275 nm in Fig. 8b-d. For the electrochemical performances, even at the high current density of 3 A/g, the MDH can still maintain a reversible capacity of 163 mAh/g after 120 cycles, delivering a retention of 71.5% (Fig. 8e) [107]. With the concept of Schottky junction and multi-heterostructure, Chu et al. fabricated SnS@C@MoS₂@NC electrodes using a two-step synthesis by thermal injection and hydrothermal method (Fig. 8f and g), and exhibited enhanced potassium storage capacity [71]. Schottky

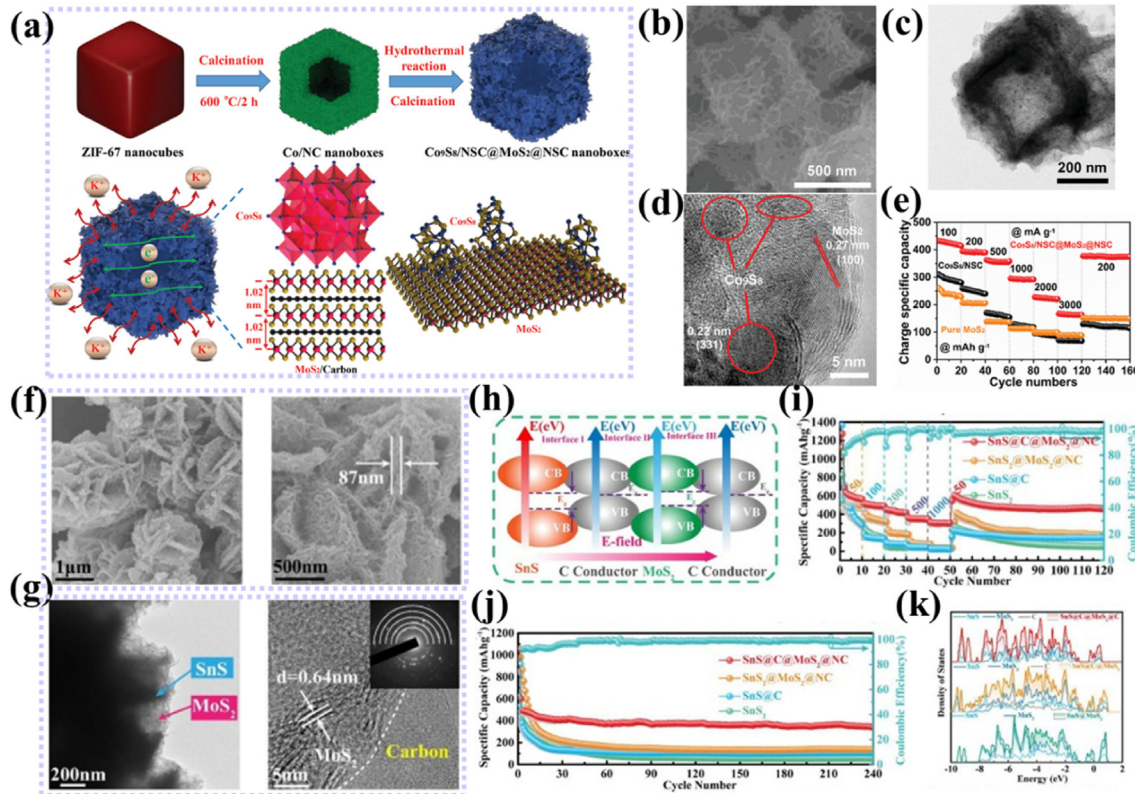


Fig. 8. (a) Schematic illustration of the preparation process and transport of electrons and K ions in the Co₃S₈/NSC@MoS₂@NSC and structural models with expanded interlayer spacing and strong chemical bonding. (b) SEM image, (c) TEM image, and (d) HRTEM images. (e) Rate capabilities of the Co₃S₈/NSC@MoS₂@NSC, Co₃S₈/NSC, and pure MoS₂ electrodes at various current densities from 100 to 3000 mA/g. Reproduced with permission from Ref. [107]. Copyright 2019, John Wiley and Sons. (f) FESEM images, (g) TEM images, and HRTEM images of SnS@C@MoS₂@NC micro flowers. (h) The built-in electric field in SnS@C@MoS₂@C. Comparison of (i) cycling performance (200 mA/g) and (j) rate performance at various current densities from 50 to 1000 mA/g. (k) The DOS of SnS@MoS₂, SnS@C@MoS₂, and SnS@C@MoS₂@C. Reproduced with permission from Ref. [71]. Copyright 2022, Elsevier.

junctions induced by phase boundaries with effective built-in electric fields will lead to enhanced intrinsic conductivity and thus improved rate capability. It is calculated that SnS@C@MoS₂@C exhibited a more stable adsorption energy than SnS, MoS₂, SnS@MoS₂, SnS@C@MoS₂, thereby greatly improving the adsorption capacity of K ions in Fig. 8h and k. In Fig. 8i and j, the above calculations result unambiguously consistent with the excellent rate capability and cyclability. There are some similar concept and strategy used in the recent literature, such as CoSe₂–Cu₂Se@NC [60], Co₂/CuCo₂S₄@NCs [108], Sb@Sb₂O₃@N–3DCHs [61], Fe₇S₈/C@d–MoS₂ [109].

4.5. Summary on the effects of different synthetic strategies for MDHs

There are many synthetic strategies for fabricating heterostructure, including hydrothermal/solvothermal, solid sintering (sulfidation/selenidation/tellurication), CVD, sol-gel/polyesterification, hot injection with a reductant, chemical precipitation, etc. (Table 1). In typical, one or two-step hydrothermal and solvothermal methods are usually used to synthesize the heterostructure, which can react under high pressure, but lower temperature (temp. range: 120–220 °C) condition compared to sintering and CVD. Nevertheless, the one-pot synthesis may affect the purity of target materials due to all the precursors are mixed in the same system. The coprecipitation method is used for producing MOF, which is a metal-based precursor, and its required temperature ranged from room temperature to 100 °C. However, most

fabrications after first-step proceed are high-temperature annealing process, which is sulfidation/selenidation steps. During the higher temperature (>350 °C), we need to be concern about the phase and morphology variation of original material. In addition, the high-temperature solid sintering without shape-controlled step would result in the formation of bulk materials rather than nanostructure. Although the sol-gel strategy is conducted through polyesterification reaction at a temperature of 140–180 °C, the polymer resin containing the metal complex would still proceed with the subsequent carbonization and reduction reaction under 500 °C. Therefore, choosing a rational strategy at a suitable temperature, great purity, unique morphology, or even stable carbon scaffold, etc., requires trade-offs as well as trial and error.

5. Conclusion and outlook

Numerous challenges of PIBs, including severe volume changes, slow kinetic reactions, poor electrical conductivity, and slow ionic diffusion, can be addressed through rational design strategies for covalent and vdW heterostructures. In this minireview, we summarize and list suitable modification methods and characterizations of MDHs, categorized into 2D–2D, 1D–2D, 0D–based, and multidimensional. Combination of different dimensional materials can synergistically promote the feasible utilization of energy storage and exhibit advantages in kinetic reactions involving ion adsorption and diffusion. Due to the different properties of semiconductors, insulators, and conductors, the built-in fields and corresponding bandgaps of MDHs are affected. The improved electric

and ionic conductivity of heterostructures reduces the volume variation and accelerates K-ion transportation in PIBs. Most importantly, the theoretical simulations also provide the evidence for advanced electrochemical performances, involving rate capability, cyclability, diffusion barrier, adsorption energy, etc. Benefiting from the formation of heterointerface, the band structure, and intrinsic properties are significantly changed and promoted. With the excellent studies in recent years, the state-of-art design and corresponding performance have been clearly proposed and can be applied to other electrochemical storage systems, such as zinc-ion, calcium-ion, and aluminum-ion batteries. To further promote the development of heterostructured materials, we propose some feasible research directions, highlighted below.

5.1. Engineering the rational and controllable synthesis methods

Due to the unique properties of MDHs, including covalent or vdW epitaxy, rational synthesis strategies with simple fabrication processes, such as low temperature, short synthesis time, atmospheric pressure, etc., are regarded as important targets and even become mainstream with high-performance potassium-ion storages. The contact facet, geometric topography, and specific growth direction can be more facile to be tuned by experimental parameters and controllable factors. With tunable and rational strategies, the high-quality MDHs with functional designs can further scale up to meet the high-quantity demand. Therefore, universally controllable design methods and mechanisms could make the heteroepitaxial fabrication process easier to adopt and extend to other fields of electrochemistry for next-generation energy storage.

5.2. Optimizing the electrochemical performance with other components

The optimized other components, such as electrolyte, binder, and conductive agent, can promote the cycling stability of heterostructure. Wu et al. proposed a fundamental study of mechanical strength of binder and SEI film formation, maximizing the electrochemical performance benefited from the cross-linked binder and the stable SEI layers derived from the electrolyte [111]. Different electrolyte solvents and salts are a significant factor to form a robust SEI layer surrounding the electrodes, affecting the Columbic efficiency of alloy and conversion anodes during charge-discharge process [112]. Besides, the improvement of the conductive agent contained in the electrode slurry can greatly increase the conductivity and electric contact of the whole electrode system. Chen et al. used a mix of super P and graphene as the conductive agent reduces the charge transfer resistance during cycling, increases the specific capacity, and enables the battery to maintain excellent cycling stability [113]. Therefore, we can simultaneously engineer the MDHs and improve the other electrode components to accomplish the long-term cyclability with an optimized system.

5.3. In-depth insight into MDHs through advanced characterization methods

The ex-situ and in-situ XRD contour plot or Raman spectroscopy are often performed on evolution of electrochemical mechanism. Furthermore, advanced *operando* techniques can be applied to observe changes in the heterojunction or interface during cycling. For instance, the advanced *in-situ* transmission X-ray microscopy (TXM) or TEM may be a method to clearly reveal morphological changes consistent with phase transitions in XRD or Raman analysis. It is worth mentioning that the electrochemical reaction intermediates of the heterostructure, which contribute a great capacity, may be different from the original concept and

mechanism owing to the formation of bonds between two materials. Hence, advanced *operando* techniques should be applied to provide a comprehensive understanding of heterojunction and a design guide of MDHs.

5.4. Potassium-ion full batteries and hybrid capacitor

The most-reported literature focus on the analysis and testing of half-cell batteries. However, the feasibility of potassium-ion full batteries or hybrid capacitors is an important component in practical applications, which have high requirements and needs on the energy density and power density of full cells. The potassium-ion full batteries usually coupled with Prussian analogues or organic cathodes can display the strengths regarding the capacitive storage ability, reflecting the amount of energy density. The normal capacitors are constructed by symmetry cells, while the novel hybrid capacitor is composed of active carbon and high-capacity anode. Benefiting from the interface modification and junction enhancement of heterostructures, the electric resistance and ion diffusion barrier have been decreased. The rapid kinetic reaction and structural stability of metal chalcogenide and oxides are significantly activated and improved, promoting the storage efficiency and diffusion capability. Both capacity contribution and ion transportation of K ions in anode materials will affect the performances of energy and power density. As full cells are assembled and demonstrated in Ragone plot, the utilization of potassium-ion systems will be more refined to develop next-generation storage devices.

Declaration of competing interest

The authors declare that they have no known competing financial interests or personal relationships that could have appeared to influence the work reported in this paper.

Acknowledgments

This work was financially supported by the financial support Young Scholar Fellowship Program by Ministry of Science and Technology, Taiwan (MOST 111-2628-E-007-008). All graphics and figures are attained with permission.

References

- [1] M. Aneke, M. Wang, Energy storage technologies and real life applications—A state of the art review, *Appl. Energy* 179 (2016) 350–377.
- [2] S. Koohi-Fayegh, M.A. Rosen, A review of energy storage types, applications and recent developments, *J. Energy Storage* 27 (2020) 101047.
- [3] R. Rajagopalan, Y. Tang, X. Ji, C. Jia, H. Wang, Advancements and challenges in potassium ion batteries: a comprehensive review, *Adv. Funct. Mater.* 30 (2020) 1909486.
- [4] K.-T. Chen, Y.-C. Yang, L.-M. Lyu, M.-Y. Lu, H.-Y. Tuan, In situ formed robust submicron-sized nanocrystalline aggregates enable highly-reversible potassium ion storage, *Nano Energy* 88 (2021) 106233.
- [5] J. Wang, Z. Liu, J. Zhou, K. Han, B. Lu, Insights into metal/metalloid-based alloying anodes for potassium ion batteries, *ACS Mater. Lett.* 3 (2021) 1572–1598.
- [6] K.-T. Chen, H.-Y. Tuan, Bi–Sb nanocrystals embedded in phosphorus as high-performance potassium ion battery electrodes, *ACS Nano* 14 (2020) 11648–11661.
- [7] Y.-Y. Hsieh, K.-T. Chen, H.-Y. Tuan, A synergistic SnSb-amorphous carbon composites prepared from polyesterification process as an ultrastable potassium-ion battery anode, *Chem. Eng. J.* 15 (2021) 130451.
- [8] K.-T. Chen, S. Chong, L. Yuan, Y.-C. Yang, H.-Y. Tuan, Conversion-alloying dual mechanism anode: nitrogen-doped carbon-coated Bi_2Se_3 wrapped with graphene for superior potassium-ion storage, *Energy Storage Mater.* 39 (2021) 239–249.
- [9] C.-B. Chang, K.-T. Chen, H.-Y. Tuan, Large-scale synthesis of few-layered copper antimony sulfide nanosheets as electrode materials for high-rate potassium-ion storage, *J. Colloid Interface Sci.* 608 (2022) 984–994.

- [10] C.-Y. Tsai, C.-H. Chang, T.-L. Kao, K.-T. Chen, H.-Y. Tuan, Shape matters: SnPo₉₄ teardrop nanorods with boosted performance for potassium ion storage, *Chem. Eng. J.* 417 (2021) 128552.
- [11] S.-B. Huang, Y.-Y. Hsieh, K.-T. Chen, H.-Y. Tuan, Flexible nanostructured potassium-ion batteries, *Chem. Eng. J.* 416 (2021) 127697.
- [12] C.-H. Chang, K.-T. Chen, Y.-Y. Hsieh, C.-B. Chang, H.-Y. Tuan, Crystal facet and architecture engineering of metal oxide nanonetwork anodes for high-performance potassium ion batteries and hybrid capacitors, *ACS Nano* 16 (2022) 1486–1501.
- [13] Z. Li, R. Sun, Z. Qin, X. Liu, C. Wang, H. Fan, Y. Zhang, S. Lu, Recent progress of nanostructured metal chalcogenides and their carbon-based hybrids for advanced potassium battery anodes, *Mater. Chem. Front.* 5 (2021) 4401–4423.
- [14] C. Li, S. Dong, R. Tang, X. Ge, Z. Zhang, C. Wang, Y. Lu, L. Yin, Heteroatomic interface engineering in MOF-derived carbon heterostructures with built-in electric-field effects for high performance Al-ion batteries, *Energy Environ. Sci.* 11 (2018) 3201–3211.
- [15] H. Li, C. Chen, Y. Yan, T. Yan, C. Cheng, D. Sun, L. Zhang, Utilizing the built-in electric field of p–n junctions to spatially propel the stepwise polysulfide conversion in lithium–sulfur batteries, *Adv. Mater.* 33 (2021) 2105067.
- [16] Y.J. Hong, C.-H. Lee, Van der Waals heteroepitaxy of semiconductor nanowires, *Semiconductors and Semimetals*, Elsevier, 2015, pp. 125–172.
- [17] P. Xiong, F. Zhang, X. Zhang, S. Wang, H. Liu, B. Sun, J. Zhang, Y. Sun, R. Ma, Y. Bando, C. Zhou, Z. Liu, T. Sasaki, G. Wang, Strain engineering of two-dimensional multilayered heterostructures for beyond-lithium-based rechargeable batteries, *Nat. Commun.* 11 (2020) 1–12.
- [18] T. Shen, J.-C. Ren, X. Liu, S. Li, W. Liu, van der Waals stacking induced transition from Schottky to ohmic contacts: 2D metals on multilayer InSe, *J. Am. Chem. Soc.* 141 (2019) 3110–3115.
- [19] X. Ding, Y. Zhao, H. Xiao, L. Qiao, Engineering Schottky-to-Ohmic contact transition for 2D metal–semiconductor junctions, *Appl. Phys. Lett.* 118 (2018), 091601.
- [20] Y. Tak, S.J. Hong, J.S. Lee, K. Yong, Solution-based synthesis of a CdS nanoparticle/ZnO nanowire heterostructure array, *Cryst. Growth Des.* 9 (2009) 2627–2632.
- [21] W. Zheng, W. Feng, X. Zhang, X. Chen, G. Liu, Y. Qiu, T. Hasan, P. Tan, P.A. Hu, Anisotropic growth of nonlayered CdS on MoS₂ monolayer for functional vertical heterostructures, *Adv. Funct. Mater.* 26 (2016) 2648–2654.
- [22] D. Perovic, M. Castell, A. Howie, C. Lavoie, T. Tiedje, J. Cole, Field-emission SEM imaging of compositional and doping layer semiconductor superlattices, *Ultramicroscopy* 58 (1995) 104–113.
- [23] J. Jing, J. Yang, W. Li, Z. Wu, Y. Zhu, Construction of interfacial electric field via dual-porphyrin heterostructure boosting photocatalytic hydrogen evolution, *Adv. Mater.* 34 (2022) 2106807.
- [24] Y. Zheng, A. Kumamoto, K. Hisama, K. Otsuka, G. Wickerson, Y. Sato, M. Liu, T. Inoue, S. Chiashi, D.-M. Tang, Q. Zhang, A. Anisimov, E.I. Kauppinen, Y. Li, K. Suenaga, S. Maruyama, R. Xiang, One-dimensional van der Waals heterostructures: growth mechanism and handedness correlation revealed by nondestructive TEM, *Proc. Natl. Acad. Sci.* 118 (2021), e2107295118.
- [25] Q. Li, X. Xu, J. Guo, J.P. Hill, H. Xu, L. Xiang, C. Li, Y. Yamauchi, Y. Mai, Two-dimensional MXene-polymer heterostructure with ordered in-plane meso-channels for high-performance capacitive deionization, *Angew. Chem.* 133 (2021) 26732–26738.
- [26] J. Li, X. Yang, Y. Liu, B. Huang, R. Wu, Z. Zhang, B. Zhao, H. Ma, W. Dang, Z. Wei, K. Wang, Z. Lin, X. Yan, M. Sun, B. Li, X. Pan, J. Luo, G. Zhang, Y. Liu, Y. Huang, X. Duan, X. Duan, General synthesis of two-dimensional van der Waals heterostructure arrays, *Nature* 579 (2020) 368–374.
- [27] D. Wu, L. Xie, X. Xu, J. He, High thermoelectric performance achieved in GeTe–Bi₂Te₃ pseudo-binary via van der Waals gap-induced hierarchical ferroelectric domain structure, *Adv. Funct. Mater.* 29 (2019) 1806613.
- [28] G.-J. Lai, L.-M. Lyu, Y.-S. Huang, G.-C. Lee, M.-P. Lu, T.-P. Perng, M.-Y. Lu, L.-J. Chen, Few-layer WS₂–MoS₂ in-plane heterostructures for efficient photocatalytic hydrogen evolution, *Nano Energy* 81 (2021) 105608.
- [29] W.-J. Chun, A. Ishikawa, H. Fujisawa, T. Takata, J.N. Kondo, M. Hara, M. Kawai, Y. Matsumoto, K. Domen, Conduction and valence band positions of Ta₂O₅, TaON, and Ta₃N₅ by UPS and electrochemical methods, *J. Phys. Chem. B* 107 (2003) 1798–1803.
- [30] P. Makula, M. Pacia, W. Macyk, How to Correctly Determine the Band Gap Energy of Modified Semiconductor Photocatalysts Based on UV–Vis Spectra, ACS Publications, 2018, pp. 6814–6817.
- [31] F. Meng, J. Li, S.K. Cushing, M. Zhi, N. Wu, Solar hydrogen generation by nanoscale p–n junction of p-type molybdenum disulfide/n-type nitrogen-doped reduced graphene oxide, *J. Am. Chem. Soc.* 135 (2013) 10286–10289.
- [32] H. Kong, C. Yan, C. Lv, J. Pei, G. Chen, Electric field effect in a Co₃O₄/TiO₂ p–n junction for superior lithium-ion storage, *Mater. Chem. Front.* 3 (2019) 909–915.
- [33] C.-J. Chang, M.-C. Teng, J. Chen, Y.-G. Lin, C.-Y. Chen, Microwave solvothermal synthesis of cubic MnS@ Ag₂S core-shell photocatalysts with improved charge separation and photocatalytic activity, *Appl. Surf. Sci.* 558 (2021) 149875.
- [34] M. Myers, F.L.M. Khir, M.A. Home, C. Mennell, J. Gillbanks, A. Tadich, M.V. Baker, B.D. Nener, G. Parish, XPS/NEXAFS spectroscopic and conductance studies of glycine on AlGaN/GaN transistor devices, *Appl. Surf. Sci.* 435 (2018) 23–30.
- [35] H. Liu, Z.X. Liu, S. Wang, J. Huang, H. Ju, Q. Chen, J. Yu, H. Chen, C.Z. Li, Boosting organic–metal oxide heterojunction via conjugated small molecules for efficient and stable nonfullerene polymer solar cells, *Adv. Energy Mater.* 9 (2019) 1900887.
- [36] S. Moon, S.-J. Chang, Y. Kim, O.F.N. Okello, J. Kim, J. Kim, H.-W. Jung, H.-K. Ahn, D.-S. Kim, S.-Y. Choi, J.-D. Lee, J.-w. Lim, J.-K. Kim, Van der Waals heterostructure of hexagonal boron nitride with an AlGaN/GaN epitaxial wafer for high-performance radio frequency applications, *ACS Appl. Mater. Interfaces* 13 (2021) 59440–59449.
- [37] C. Ye, Y. Jiao, H. Jin, A.D. Slattery, K. Davey, H. Wang, S.Z. Qiao, 2D Mon-VN heterostructure to regulate polysulfides for highly efficient lithium-sulfur batteries, *Angew. Chem. Int. Ed.* 57 (2018) 16703–16707.
- [38] C. Lee, H. Yan, L.E. Brus, T.F. Heinz, J. Hone, S. Ryu, Anomalous lattice vibrations of single-and few-layer MoS₂, *ACS Nano* 4 (2010) 2695–2700.
- [39] L. Liang, V. Meunier, First-principles Raman spectra of MoS₂, WS₂ and their heterostructures, *Nanoscale* 6 (2014) 5394–5401.
- [40] N. Li, Y. Wen, R. Cheng, L. Yin, F. Wang, J. Li, T.A. Shifa, L. Feng, Z. Wang, J. He, Strongly coupled van der Waals heterostructures for high-performance infrared phototransistor, *Appl. Phys. Lett.* 114 (2019) 103501.
- [41] J.-J. Tao, J. Jiang, S.-N. Zhao, Y. Zhang, X.-X. Li, X. Fang, P. Wang, W. Hu, Y.H. Lee, H.-L. Lu, D.-w. Zhang, Fabrication of 1D Te/2D ReS₂ mixed-dimensional van der Waals pn heterojunction for high-performance phototransistor, *ACS Nano* 15 (2021) 3241–3250.
- [42] D. Sarma, P.K. Santra, S. Mukherjee, A. Nag, X-ray photoelectron spectroscopy: a unique tool to determine the internal heterostructure of nanoparticles, *Chem. Mater.* 25 (2013) 1222–1232.
- [43] L. Hu, C. Dai, H. Liu, Y. Li, B. Shen, Y. Chen, S.J. Bao, M. Xu, Double-shelled NiO-NiCo₂O₄ heterostructure@ carbon hollow nanocages as an efficient sulfur host for advanced lithium–sulfur batteries, *Adv. Energy Mater.* 8 (2018) 1800709.
- [44] M. Ma, S. Zhang, Y. Yao, H. Wang, H. Huang, R. Xu, J. Wang, X. Zhou, W. Yang, Z. Peng, X. Wu, Y. Hou, Y. Yu, Heterostructures of 2D molybdenum dichalcogenide on 2D nitrogen-doped carbon: superior potassium-ion storage and insight into potassium storage mechanism, *Adv. Mater.* 32 (2020) 2000958.
- [45] C.R. Wie, High resolution X-ray diffraction characterization of semiconductor structures, *Mater. Sci. Eng. R* 13 (1994) 1–56.
- [46] Y. Chen, D.D. Fong, F.W. Herbert, J. Rault, J.-P. Rueff, N. Tsvetkov, B. Yildiz, Modified oxygen defect chemistry at transition metal oxide heterostructures probed by hard X-ray photoelectron spectroscopy and X-ray diffraction, *Chem. Mater.* 30 (2018) 3359–3371.
- [47] V. Harutyunyan, A. Aivazyan, E. Weber, Y. Kim, Y. Park, S. Subramanya, High-resolution x-ray diffraction strain-stress analysis of GaN/sapphire heterostructures, *J. Phys. D Appl. Phys.* 34 (2001) A35.
- [48] C. He, J. Zhang, W. Zhang, T. Li, GeSe/BP van der Waals heterostructures as promising anode materials for potassium-ion batteries, *J. Phys. Chem. C* 123 (2019) 5157–5163.
- [49] H. Shan, J. Qin, Y. Ding, H.M.K. Sari, X. Song, W. Liu, Y. Hao, J. Wang, C. Xie, J. Zhang, X. Li, Controllable heterojunctions with a semicoherent phase boundary boosting the potassium storage of CoSe₂/FeSe₂, *Adv. Mater.* 33 (2021) 2102471.
- [50] C. Ma, H. Yang, Z. Xu, Z. Fu, Y. Xie, H. Zhang, M. Hong, Z. Ma, H. Xiong, X.-Z. Yuan, Insights into high capacity and ultrastable carbonaceous anodes for potassium-ion storage via a hierarchical heterostructure, *J. Mater. Chem. B* 8 (2020) 2836–2842.
- [51] X. Ge, H. Di, P. Wang, X. Miao, P. Zhang, H. Wang, J. Ma, L. Yin, Metal–organic framework-derived nitrogen-doped cobalt nanocluster inlaid porous carbon as high-efficiency catalyst for advanced potassium–sulfur batteries, *ACS Nano* 14 (2020) 16022–16035.
- [52] R. Xu, Y. Yao, H. Wang, Y. Yuan, J. Wang, H. Yang, Y. Jiang, P. Shi, X. Wu, Z. Peng, Z.-s. Wu, j. Lu, Y. Yu, Unraveling the nature of excellent potassium storage in small-molecule Se@ peapod-like N-doped carbon nanofibers, *Adv. Mater.* 32 (2020) 2003879.
- [53] L. Cao, B. Luo, B. Xu, J. Zhang, C. Wang, Z. Xiao, S. Li, Y. Li, B. Zhang, G. Zou, H. Hou, X. Ou, X. Ji, Stabilizing intermediate phases via efficient entrapment effects of layered VS₄/SnS@ C heterostructure for ultralong lifespan potassium-ion batteries, *Adv. Funct. Mater.* 31 (2021) 2103802.
- [54] B. Chen, J. Ding, X. Bai, H. Zhang, M. Liang, S. Zhu, C. Shi, L. Ma, E. Liu, N. Zhao, Engineering pocket-like graphene–shell encapsulated FeS₂: inhibiting polysulfides shuttle effect in potassium-ion batteries, *Adv. Funct. Mater.* (2021) 2109899.
- [55] R. Jayan, M.M. Islam, Mechanistic insights into interactions of polysulfides at VS₂ interfaces in Na–S batteries: a DFT study, *ACS Appl. Mater. Interfaces* 13 (2021) 35848–35855.
- [56] J. Pu, W. Gong, Z. Shen, L. Wang, Y. Yao, G. Hong, CoNiO₂/Co₃N heterostructure nanowires assisted polysulfide reaction kinetics for improved lithium–sulfur batteries, *Adv. Sci.* 9 (2022) 2104375.
- [57] A.F. Oliveira, G. Seifert, T. Heine, H.A. Duarte, Density-functional based tight-binding: an approximate DFT method, *J. Braz. Chem. Soc.* 20 (2009) 1193–1205.
- [58] Z. Xia, X. Chen, H. Ci, Z. Fan, Y. Yi, W. Yin, N. Wei, J. Cai, Y. Zhang, J. Sun, Designing N-doped graphene/ReSe₂/Ti₃C₂ MXene heterostructure frameworks as promising anodes for high-rate potassium-ion batteries, *J. Energy Chem.* 53 (2021) 155–162.
- [59] Y. Li, C. Yang, F. Zheng, Q. Pan, Y. Liu, G. Wang, T. Liu, J. Hu, M. Liu, Design of TiO₂eC hierarchical tubular heterostructures for high performance potassium ion batteries, *Nano Energy* 59 (2019) 582–590.
- [60] X. Liu, Z. Niu, Y. Xu, Z. Zhao, C. Li, Y. Yi, H. Guan, S. Zhang, X. Pei, D. Li, Rational design heterostructured bimetallic selenides for high capacity and durability sodium/potassium-ion storage, *Chem. Eng. J.* 430 (2022) 133176.

- [61] B. Chen, L. Yang, X. Bai, Q. Wu, M. Liang, Y. Wang, N. Zhao, C. Shi, B. Zhou, C. He, Heterostructure engineering of core-shelled Sb@Sb₂O₃ encapsulated in 3D N-doped carbon hollow-spheres for superior sodium/potassium storage, *Small* 17 (2021) 2006824.
- [62] J. Wang, Z. Xu, J.C. Eloi, M.M. Titirici, S.J. Eichhorn, Ice-templated, sustainable carbon aerogels with hierarchically tailored channels for sodium-and potassium-ion batteries, *Adv. Funct. Mater.* (2022) 2110862.
- [63] F. Qiao, J. Wang, Y. Zhu, X. Tan, X. Wang, Q. An, Cheese-Like Porous SnP₂O₇ composite as a long-life and high-rate anode material for potassium-ion batteries, *Chem. Eng. J.* 439 (2022) 135777.
- [64] X. Xu, F. Li, D. Zhang, Z. Liu, S. Zuo, Z. Zeng, J. Liu, Self-sacrifice template construction of uniform yolk-shell ZnS@C for superior alkali-ion storage, *Adv. Sci.* (2022) 2200247.
- [65] Y. Shi, L. Wang, D. Zhou, T. Wu, Z. Xiao, A flower-like Sb₄O₅Cl₂ cluster-based material as anode for potassium ion batteries, *Appl. Surf. Sci.* 583 (2022) 152509.
- [66] C.-C. Chuang, Y.-Y. Hsieh, W.-C. Chang, H.-Y. Tuan, Phosphorus-sulfur/grapheene composites as flexible lithium-sulfur battery cathodes with super high volumetric capacity, *Chem. Eng. J.* 387 (2020) 123904.
- [67] J. Wang, W. Yan, J. Zhang, High area capacity and dendrite-free anode constructed by highly potassiophilic Pd/Cu current collector for low-temperature potassium metal battery, *Nano Energy* 96 (2022) 107131.
- [68] J. Wu, S. Liu, Y. Rehman, T. Huang, J. Zhao, Q. Gu, J. Mao, Z. Guo, Phase engineering of nickel sulfides to boost sodium-and potassium-ion storage performance, *Adv. Funct. Mater.* 31 (2021) 2010832.
- [69] M. Ubaid, A. Aziz, B.S. Pujari, Two-dimensional C₃N/blue phosphorene vdW heterostructure for Li, Na and K-ion batteries, *New J. Chem.* 45 (2021) 12647–12654.
- [70] Z. Mansouri, A. Sibari, A. Al-Shami, S. Lahbabí, A. El Kenz, A. Benyoussef, A. El Fatimi, O. Mounkachi, Graphene/Phosphorene nano-heterostructure as a potential anode material for (K/Na)-ion batteries: insights from DFT and AIMD, *Comput. Mater. Sci.* 202 (2022) 110936.
- [71] J. Chu, K. Han, Q. Yu, H. Wang, K. Xi, F. Lai, J. Zhang, Y. Bao, Schottky junction and multiheterostructure synergistically enhance rate performance and cycling stability, *Chem. Eng. J.* 430 (2022) 132994.
- [72] S. Liang, Z. Yu, T. Ma, H. Shi, Q. Wu, L. Ci, Y. Tong, J. Wang, Z. Xu, Mechanistic insights into the structural modulation of transition metal selenides to boost potassium ion storage stability, *ACS Nano* 15 (2021) 14697–14708.
- [73] A. Agrawal, S. Janakiraman, K. Biswas, A. Venimadhav, S. Srivastava, S. Ghosh, Understanding the improved electrochemical performance of nitrogen-doped hard carbons as an anode for sodium ion battery, *Electrochim. Acta* 317 (2019) 164–172.
- [74] Q. Peng, F. Ling, H. Yang, P. Duan, R. Xu, Q. Wang, Y. Yu, Boosting potassium storage performance via construction of NbSe₂-based misfit layered chalcogenides, *Energy Storage Mater.* 39 (2021) 265–270.
- [75] J. Wang, B. Wang, B. Lu, Nature of novel 2D van der Waals heterostructures for superior potassium ion batteries, *Adv. Energy Mater.* 10 (2020) 2000884.
- [76] H. Liu, Y. He, H. Zhang, S. Wang, K. Cao, Y. Jiang, X. Liu, Q.-S. Jing, Heterostructure engineering of ultrathin SnS₂/Ti_xC₂T_x nanosheets for high-performance potassium-ion batteries, *J. Colloid Interface Sci.* 606 (2022) 167–176.
- [77] B. Luo, P. Wu, J. Zhang, L. Cao, C. Wang, B. Lu, B. Zhang, X. Ou, Van der Waals heterostructure engineering by 2D space-confinement for advanced potassium-ion storage, *Nano Res.* (2021) 1–10.
- [78] B. Yu, Y. Ji, X. Hu, Y. Liu, J. Yuan, S. Lei, G. Zhong, Z. Weng, H. Zhan, Z. Wen, Heterostructured Cu₂₅@ZnS/C composite with fast interfacial reaction kinetics for high-performance 3D-printed Sodium-Ion batteries, *Chem. Eng. J.* 430 (2022) 132993.
- [79] X. Huang, Y. Zhao, K. Lin, X. Liu, J. Zhao, H. Chen, Z. Wang, X. Hou, Vertical 2-dimensional heterostructure SnS-SnS₂ with built-in electric field on rGO to accelerate charge transfer and improve the shuttle effect of polysulfides, *J. Colloid Interface Sci.* 608 (2022) 120–130.
- [80] H. Huang, J. Cui, G. Liu, R. Bi, L. Zhang, Carbon-coated MoSe₂/MXene hybrid nanosheets for superior potassium storage, *ACS Nano* 13 (2019) 3448–3456.
- [81] R. Agarwal, Heterointerfaces in semiconductor nanowires, *Small* 4 (2008) 1872–1893.
- [82] H. Pan, Y.P. Feng, Semiconductor nanowires and nanotubes: effects of size and surface-to-volume ratio, *ACS Nano* 2 (2008) 2410–2414.
- [83] J.K. Hyun, S. Zhang, L.J. Lauhon, Nanowire heterostructures, *Annu. Rev. Mater. Res.* 43 (2013) 451–479.
- [84] D. Samantaray, A. Kumar, P. Ghosh, D. Chatterjee, P. Bellare, M. Pandey, U. Chandni, N. Ravishankar, Solution phase synthesis of radial-axial heterostructured nanowires with coherent interfaces, *J. Phys. Chem. C* 125 (2021) 3102–3109.
- [85] S. Wang, S. Zhao, X. Guo, G. Wang, 2D material-based heterostructures for rechargeable batteries, *Adv. Energy Mater.* 12 (2021) 2100864.
- [86] J. Cao, Z. Sun, J. Li, Y. Zhu, Z. Yuan, Y. Zhang, D. Li, L. Wang, W. Han, Microbe-assisted assembly of Ti₃C₂T_x MXene on fungi-derived nanoribbon heterostructures for ultrastable sodium and potassium ion storage, *ACS Nano* 15 (2021) 3423–3433.
- [87] P. Vishnuprakash, C. Nithya, M. Premalatha, Exploration of V₂O₅ nanorod@rGO heterostructure as potential cathode material for potassium-ion batteries, *Electrochim. Acta* 309 (2019) 234–241.
- [88] X. Xu, Y. Zhang, H. Sun, J. Zhou, Z. Liu, Z. Qiu, D. Wang, C. Yang, Q. Zeng, Z. Peng, S. Guo, Orthorhombic cobalt ditelluride with Te vacancy defects anchoring on elastic MXene enables efficient potassium-ion storage, *Adv. Mater.* 33 (2021) 2100272.
- [89] L. Xu, Y. Wang, C. Lin, X. Xia, X. Chen, P. Xiong, Q. Chen, M. Wei, Q. Qian, L. Zeng, Algal residues-engaged formation of novel WVO₄/V₃Se₄ hybrid nanostructure with carbon fiber confinement for enhanced long-term cycling stability in sodium/potassium storage, *J. Alloys Compd.* 892 (2022) 162177.
- [90] J. Cao, J. Li, D. Li, Z. Yuan, Y. Zhang, V. Shulga, Z. Sun, W. Han, Strongly coupled 2D transition metal chalcogenide-MXene-carbonaceous nanoribbon heterostructures with ultrafast ion transport for boosting sodium/potassium ions storage, *Micro & Nano Lett.* 13 (2021) 1–20.
- [91] G. Suo, D. Li, L. Feng, X. Hou, X. Ye, L. Zhang, Q. Yu, Y. Yang, W.A. Wang, Construction of SnS₂/SnO₂ heterostructures with enhanced potassium storage performance, *J. Mater. Sci. Technol.* 55 (2020) 167–172.
- [92] L. Yu, G. Wang, J. Gao, J. Li, B. Peng, G. Zhang, Sacrificial nanowire catalyzed polymerization process generates hierarchical MoSe₂ grafted carbonaceous nanotubes for superior potassium ion storage, *ACS Appl. Energy Mater.* 4 (2021) 6757–6767.
- [93] H. Yin, W. Shen, H.-Q. Qu, C. Li, M.-Q. Zhu, Boosted charge transfer and Na⁺ diffusion in cooling-fins-like Sb₂Te₃–Te nano-heterostructure for long cycle life and high rate capability anode, *Nano Energy* 70 (2020) 104468.
- [94] J. Zheng, Y. Wu, Y. Sun, J. Rong, H. Li, L. Niu, Advanced anode materials of potassium ion batteries: from zero dimension to three dimensions, *Micro & Nano Lett.* 13 (2021) 1–37.
- [95] Y. Ai, Y. You, F. Wei, X. Jiang, Z. Han, J. Cui, H. Luo, Y. Li, Z. Xu, S. Xu, J. Yang, Q. Bao, C. Jing, J. Fu, J. Cheng, S. Liu, Hollow bio-derived polymer nanospheres with ordered mesopores for sodium-ion battery, *Micro & Nano Lett.* 12 (2020) 1–11.
- [96] C. Yang, F. Lv, Y. Zhang, J. Wen, K. Dong, H. Su, F. Lai, G. Qian, W. Wang, A. Hilger, Y. Xu, Y. Zhu, Y. Deng, W. Hu, I. Manke, Y. Chen, Confined Fe₂VO₄^c nitrogen-doped carbon nanowires with internal void space for high-rate and ultrastable potassium-ion storage, *Adv. Energy Mater.* 9 (2019) 1902674.
- [97] Z. Yan, J. Liu, H. Wei, X. Yang, Y. Yao, Z. Huang, H. Li, Y. Kuang, J. Ma, H. Zhou, Embedding FeS nanodots into carbon nanosheets to improve the electrochemical performance of anode in potassium ion batteries, *J. Colloid Interface Sci.* 593 (2021) 408–416.
- [98] L. Cao, B. Zhang, H. Xia, C. Wang, B. Luo, X. Fan, J. Zhang, X. Ou, Hierarchical chrysanthemum-like MoS₂/Sb heterostructure encapsulated into N-doped graphene framework for superior potassium-ion storage, *Chem. Eng. J.* 387 (2020) 124060.
- [99] S. Chabi, C. Peng, D. Hu, Y. Zhu, Ideal three-dimensional electrode structures for electrochemical energy storage, *Adv. Mater.* 26 (2014) 2440–2445.
- [100] Q. Jiang, S. Hu, L. Wang, Z. Huang, H.-J. Yang, X. Han, Y. Li, C. Lv, Y.-S. He, T. Zhou, Boosting potassium storage in nanosheet assembled MoSe₂ hollow sphere through surface decoration of MoO₂ nanoparticles, *Appl. Surf. Sci.* 505 (2020) 144573.
- [101] Q. Jiang, L. Wang, W. Zhao, X. Xu, Z. Li, Y. Li, T. Zhou, J. Hu, Carbon dots decorated on the ultrafine metal sulfide nanoparticles implanted hollow layered double hydroxides nanocages as new-type anodes for potassium-ion batteries, *Chem. Eng. J.* 433 (2021) 133539.
- [102] Y. Li, F. Wu, J. Qian, M. Zhang, Y. Yuan, Y. Bai, C. Wu, Metal chalcogenides with heterostructures for high-performance rechargeable batteries, *Small Science* 1 (2021) 2100012.
- [103] D.-Y. Jo, S.-K. Park, Constructing hollow CoSe₂/SnSe₂ heterostructures covered with N-doped carbon shell for high-efficiency potassium-ion storage, *Appl. Surf. Sci.* 571 (2022) 151293.
- [104] C. Liu, Y. Xia, Y. Zhang, Q.-Y. Zhou, H.-B. He, F.-D. Yu, Z.-R. Wu, J. Liu, X.-L. Sui, D.-M. Gu, Z.-B. Wang, Pseudocapacitive crystalline MnCo₂O₄⁵ and amorphous MnCo₂S₄ core/shell heterostructure with graphene for high-performance K-ion hybrid capacitors, *ACS Appl. Mater. Interfaces* 12 (2020) 54773–54781.
- [105] J.H. Choi, G.D. Park, Y.C. Kang, Potassium-ion storage mechanism of MoS₂-WS₂-C microspheres and their excellent electrochemical properties, *Chem. Eng. J.* 408 (2021) 127278.
- [106] Y. Qin, Y. Zhang, J. Wang, J. Zhang, Y. Zhai, H. Wang, D. Li, Heterogeneous structured Bi₂S₃/MoS₂@NC nanoclusters: exploring the superior rate performance in sodium/potassium ion batteries, *ACS Appl. Mater. Interfaces* 12 (2020) 42902–42910.
- [107] C. Yang, J. Feng, Y. Zhang, Q. Yang, P. Li, T. Arlt, F. Lai, J. Wang, C. Yin, W. Wang, G. Qian, L. Cui, W. Yang, Y. Chen, I. Manke, Multidimensional integrated chalcogenides nanoarchitecture achieves highly stable and ultrafast potassium-ion storage, *Small* 15 (2019) 1903720.
- [108] G. Suo, S.M. Ahmed, Y. Cheng, J. Zhang, Z. Li, X. Hou, Y. Yang, X. Ye, L. Feng, L. Zhang, Q. Yu, Heterostructured CoS₂/CuCo₂S₄@N-doped carbon hollow sphere for potassium-ion batteries, *J. Colloid Interface Sci.* 608 (2022) 275–283.
- [109] W. Li, D. Wang, Z. Gong, Z. Yin, X. Guo, J. Liu, C. Mao, Z. Zhang, G. Li, A robust strategy for engineering Fe₇S₈/C hybrid nanocages reinforced by defect-rich MoS₂ nanosheets for superior potassium-ion storage, *ACS Nano* 14 (2020) 16046–16056.

- [110] X. Kuai, K. Li, J. Chen, H. Wang, J. Yao, C.-L. Chiang, T. Liu, H. Ye, J. Zhao, Y.-G. Lin, L. Zhang, V. Nicolosi, L. Gao, Interfacial engineered vanadium oxide nanoheterostructures synchronizing high-energy and long-term potassium-ion storage, *ACS Nano* 16 (2022) 1502–1510.
- [111] J. Wu, Q. Zhang, S. Liu, J. Long, Z. Wu, W. Zhang, W.K. Pang, V. Sencadas, R. Song, W. Song, Synergy of binders and electrolytes in enabling microsized alloy anodes for high performance potassium-ion batteries, *Nano Energy* 77 (2020) 105118.
- [112] C. Bommier, X. Ji, Electrolytes, SEI formation, and binders: a review of nonelectrode factors for sodium-ion battery anodes, *Small* 14 (2018) 1703576.
- [113] H. Chen, H. Zhang, Y. Wu, T. Zhang, Y. Guo, Q. Zhang, Y. Zeng, J. Lu, Nanostructured Nb₂O₅ cathode for high-performance lithium-ion battery with Super-P and graphene compound conductive agents, *J. Electroanal. Chem.* 827 (2018) 112–119.